



Fluorescent Metal Nanoclusters for Bioimaging

Jie Xu and Li Shang

1 Introduction

Fluorescent metal nanoclusters (MNCs), usually consisting of several to approximately a hundred metal atoms [1], have attracted extensive attention over the past few decades. MNCs have size down to less than 2 nm, which is comparable to the Fermi wavelength of electrons [2], resulting in the break up of the continuous density of states of the particles into discrete energy levels [1, 3]. MNCs exhibit distinct optical, electronic, and chemical properties, including strong photoluminescence, excellent photostability, and good biocompatibility. These unique properties make MNCs ideal probes for many applications in biological imaging and diagnosis.

Especially, near-infrared (NIR) fluorescent MNCs are promising probes for bioimaging,

because biological tissues show very weak absorption and autofluorescence in the NIR spectrum window (650–900 nm wavelengths) [4, 5]. Also, NIR light can pass across several centimeters of heterogeneous living tissues [6]. Particularly, NIR-emitting MNC probes can alleviate several limitations of conventional NIR organic dyes and other nanoprobes like semiconductor quantum dots (QDs). Organic dyes show many drawbacks such as poor hydrophilicity and photostability, insufficient stability in biological systems, and weak multiplexing capability [7]. Most reported QDs display high inherent cytotoxicity and self-aggregation inside live cells, which limit their practical bio-applications [8].

Fluorescence lifetime imaging (FLIM) and two-photon imaging have been widely adopted in tissue and cell studies, and now have become powerful tools in early diseases diagnosis as well as guiding the disease treatment [9, 10]. Fluorescent MNCs possess much longer lifetime than that of cellular autofluorescence and most organic dyes, making them attractive markers for cellular FLIM applications, which is independent of fluorophore concentration and laser excitation intensity [11]. Although one-photon fluorescence imaging techniques are featured with good spatial resolution and high sensitivity, they hardly obtain anatomical or three-dimensional details of tumor tissues in vivo [12]. Compared to one-photon imaging, two-photon imaging is a powerful technique for enhanced tissue penetration depth

J. Xu

State Key Laboratory of Solidification Processing, Center for Nano Energy Materials, School of Materials Science and Engineering, Northwestern Polytechnical University and Shaanxi Joint Laboratory of Graphene (NPU), Xi'an, China

L. Shang (✉)

State Key Laboratory of Solidification Processing, Center for Nano Energy Materials, School of Materials Science and Engineering, Northwestern Polytechnical University and Shaanxi Joint Laboratory of Graphene (NPU), Xi'an, China

NPU-QMUL Joint Research Institute of Advanced Materials and Structures (JRI-AMAS), Northwestern Polytechnical University, Xi'an, China
e-mail: li.shang@nwpu.edu.cn

(>500 μm), low tissue autofluorescence, and self-absorption, as well as reduced photodamage [10, 13, 14]. With relatively good biocompatibility and large two-photon absorption (TPA) cross section, MNCs are also considered as ideal probes for two-photon imaging in biological system.

Besides fluorescence (FL) imaging, several other imaging techniques have also been used in the early-stage diagnosis of cancer, such as magnetic resonance imaging (MRI), X-ray computed tomography (CT), photoacoustic imaging (PAI), positron emission tomography (PET) imaging, and single-photon emission computed tomography (SPECT) [15, 16]. Each imaging modality has its own unique advantages along with intrinsic limitations [17]. For example, CT imaging can easily differentiate various tissue densities, and allow three-dimensional visual reconstructions of tissue, which suffers from poor sensitivity in soft tissues with limited density differences [18, 19]. MR imaging is able to provide high-quality 3D information of soft tissues and possesses high spatial resolution, but has the disadvantage of relatively low sensitivity [20–23]. In contrary, FL imaging has high sensitivity and resolution for imaging at the cellular level, but it cannot provide spatial resolution and 3D tissue detail [24]. Therefore, the rational combination of different modalities, known as “multimodal imaging,” is a powerful method that can provide more reliable and accurate detection of disease sites [15, 25].

In this chapter, we mainly focus on the latest progress in fluorescent MNCs probes for biological imaging. Specifically, we summarize recent advances in the synthesis and applications of fluorescent MNCs (including Au, Ag, Cu, and alloy NCs) as novel bioimaging probes, including single-modal imaging (fluorescence intensity-based imaging, FLIM, two-photon imaging, PET imaging) probes and the combination of FL imaging with several other imaging techniques to form multimodal imaging (such as FL/CT/MRI, FL/PAI/MRI, FL/SPECT, etc.) probes. In the final section, we will give a brief outlook on the challenges and opportunities for fluorescent MNCs in bioimaging applications.

2 Synthesis of Fluorescent MNCs

Up to now, many different methods have been developed to synthesize MNCs with the photoluminescence (PL) property. Generally, these approaches can be classified into two groups, “bottom-up” and “top-down” [26]. In both strategies, surface ligands or templates play an important role in defining their final properties. Therefore, in the following, we will overview each synthetic strategy based on the type of templates or capping ligands (representative examples summarized in Table 1).

2.1 Thiols

Owing to the strong interaction between thiols and Au/Ag, small thiolate molecules are the most commonly adopted stabilizers in MNC synthesis [27]. Among them, glutathione (GSH) is the most commonly adopted one, and GSH-stabilized AuNCs with a maximum emission at 780 nm could be obtained via NaBH_4 reduction. These AuNCs display strong one- and two-photon emissions, good photostability and biocompatibility [28]. By employing GSH as reducing and protecting reagent simultaneously, Zheng and coworkers [29] successfully synthesized NIR-emitting GSH-AuNCs with a core size 2.5 nm at 90 °C. Besides, water-soluble GSH-capped AuNCs were also obtained by using tetrabutylammonium borohydride (TBAB) as a mild reductant, and the yielded GSH-AuNCs showed excellent PL properties and low cytotoxicity [30]. Wu et al. [31] developed a one-pot one-cluster synthesis method to prepare monosized Ag_{14}NCs capped with GSH. They found that the fluorescence quantum yield (QY) of $\text{Ag}_{14}(\text{SG})_{11}$ NCs is strongly solvent-dependent, and the fluorescence intensity increases upon decreasing the solvent polarity or dielectric constant [32, 33]. Recently, a rapid sonochemical route to synthesize fluorescent AgNCs using hydrazine hydrate as reducing agent and GSH as capping agent was developed [34]. The as-prepared AgNCs show high photo-, time-,

Table 1 Summary of representative literatures on the synthesis of fluorescent MNCs

Metal	Capping agent	λ_{em} (nm)	QY	Size (HD)	Ref.
Au	GSH	780	–	1.1 nm*	[28]
Au	GSH	810	~0.5%	3.3 nm (2.5 nm*)	[29]
Au	GSH	650	1.6%	3.1 nm (1.9 nm*)	[30]
Au	GSH	685	1.3%	–	[49]
Ag	GSH	670	–	~1.1 nm*	[37]
Ag	GSH	720	2.8%	<2 nm*	[50]
Ag	GSH	645	8.2%	~2 nm*	[34]
Ag	GSH	640	–	~1 nm*	[31]
Cu	GSH	430	~6%	~2.2 nm*	[88]
Cu	GSH	610	5.0%	2.3 nm*	[35]
Cu	GSH	610	4.5%	2.4 nm*	[38]
Cu	GSH	585	2.1%	2.2 nm*	[89]
Ag ₂ S	GSH	679/727	0.3%, 0.1%	3.0 nm*, 3.7 nm*	[40]
Ag ₂ S	3-MPA	795	14%	7.5 nm (2.5 nm*)	[41]
AuCe	GSH	570	–	1.2–2.2 nm*	[90]
AuAg	GSH	716	3.4%	1.8 nm*	[42]
AuAg	LA	630	6.4%	3.6 nm (1.9 nm*)	[91]
AuAg	PEI-LA	680	14.56%	–	[92]
ZnAg	L-cysteine, chicken egg white protein	657	13.3%	1.8 nm*	[93]
Au	DHLA	684	~0.6%	3.2 nm	[11]
Au	DHLA	715	2.9%	3.3 nm (1.6 nm*)	[44]
Au	DHLA	720	10%	1.4 nm*	[45]
Au	DHLA	650	1–3%	<5 nm	[51]
Au	DHLA	650	~7%	2 nm*	[52]
Ag	DHLA	630	2.4%	2.1 nm (1.3 nm*)	[94]
Cu	DHLA	650	7.2%	1.9 nm*	[46]
Cu	TA	430	14%	2.2 nm*	[95]
Au	11-MUA	530	3.1%	1.33 nm*	[96]
Au	11-MUA, histidine	600	13.06%	–	[97]
Au	DPA	610	1.3%	2.14 nm (1.8 nm*)	[98]
Au	MSA/tiopronin	785	3.4%, 3.8%	~1.5 nm*	[47]
Ag	TSA	612	25%	2–5 nm*	[48]
Ag	MT	632	–	1.9 nm*	[99]
Ag	Sodium cholate	406, 430	20.1%	<1 nm*	[100]
Pt	MAA	470	18%	–	[84]
Au	BSA	710	–	~2.7 nm	[101]
Au	BSA	665	–	3.74 nm	[102]
Au	BSA	670	~6%	<3 nm*	[103]
Au	BSA	~674	~6%	~1 nm*	[104]
Au	BSA	660	~4%	1 nm*	[65]
Cd	BSA	475	2.86%	7.5 nm (~1 nm*)	[105]
Mg	BSA	465	17%	12 nm (~8.5 nm*)	[106]
Ag	HSA, BSA	620, 510	13%, 10%	2.6 nm, 2 nm	[107]
Ag	dLys	640	–	–	[64]
Au	Human transferrin	710	~7.7%	2.6 nm*	[57]
Au	Apo ferritin	665	8.2%	1.2 nm*	[58]
Au	Human transferrin	695	~4.3%	<2 nm*	[59]
Cu	Peptide	418	–	2.97 nm*	[108]
Cu	Lysozyme	450	18%	2.3 nm*	[109]

(continued)

Table 1 (continued)

Metal	Capping agent	λ_{em} (nm)	QY	Size (HD)	Ref.
Cu	Transferrin	670	6.2%	2.99 nm*	[63]
Au	Trypsin	690	6.5%	2.7 nm*	[60]
Au	Human insulin	680	~10%	5.36 nm	[61]
AuAg	Chicken egg white protein	600	5.4%	4.4 nm*	[110]
Au	Bovine pancreatic ribonuclease A	682	~12%	6.2 nm	[62]
Au	Peptide CCYTAT	677	11%	1.5 nm*	[68]
Au	Tripeptide	680	12.4%	1.6 nm*	[111]
Ag	ssDNA	705	34%	~2.5 nm*	[71]
Ag	ssDNA	700	52%	3 nm	[72]
Ag	DNA	550	17.4%	~3 nm*	[79]
Ag	DNA	550	–	~3 nm*	[80]
Ag	DNA (AS1411)	635	40.1%	1.5 nm*	[112]
Ag	C ₁₂ ssDNA	~700	17%	–	[76]
Ag	C ₂₄ ssDNA	715	14%	–	[77]
Ag	G-quadruplex (AS1411)	680	6.79%	<2 nm*	[78]
Cu	DNA	584	–	–	[113]
Au	PTMP-PMAA	~660	4.8%	<3 nm	[81]
Au	PEG	810	–	5.5 nm (2.3 nm*)	[82]
Au	PAMAM	458	25%	<2 nm*	[86]
Au	PEI-LA	696	3.13%	–	[114]
Pt	PEI	560	6.8%	2 nm (1.4 nm*)	[85]
Ag	SH-PEI	690	3%	12 nm (2.3 nm*)	[83]
Cu	PVP	518	44.67%	2.28 nm*	[115]

* core size, *HD* hydrodynamic diameter, *GSH* glutathione, *3-MPA* 3-mercaptopropionic acid, *LA* lipoic acid, *PEI* polyethyleneimine, *DHLA* dihydrolipoic acid, *TA* tannic acid, *11-MUA* 11-mercaptopundecanoic acid, *DPA* D-penicillamine, *MSA* 2-mercaptosuccinic acid, *tiopronin* N-(2-mercapto-propionyl) glycine, *TSA* thiosalicylic acid, *MT* metallothionein, *MAA* mercaptoacetic acid, *BSA* bovine serum albumin, *HSA* human serum albumin, *dLys* denatured lysozyme, *CCYTAT* H₂N–CCYRGRKKRRR–COOH, *PTMP* pentaerythritol tetrakis 3-mercaptopropionate, *PMAA* poly(methacrylic acid), *PEG* poly(ethylene glycol), *PAMAM* poly(amidoamine), *SH-PEI* thiol-polyethyleneimine, *PVP* poly(vinylpyrrolidone)

pH-, and ions-stability in aqueous solution, and have been exploited as probes for monitoring Pb²⁺ in living cells. In another work, Song and coworkers [35] reported a one-step synthetic method to prepare GSH templated CuNCs. The resultant CuNCs contain 1–3 atoms and exhibit red fluorescence (λ_{em} = 610 nm) with high QY, up to 5.0%. Interestingly, the fluorescence signal of the CuNCs is reversibly responsive to the environmental temperature in the range of 15–80 °C.

Wang and coworkers [36] proposed a different strategy to in situ biosynthesize fluorescent AuNCs inside cancer cells and tumor tissues. They found that HAuCl₄ can undergo a more rapid and efficient spontaneous reduction into AuNCs inside cancerous cells than in normal

ones, enabling self-bio-imaging of cancer cells and tumors by long-lasting fluorescent markers. Subsequently, they reported the intracellular bio-synthesis of AgNCs by cancerous cells incubated with silver ions [37]. AgNCs were spontaneously biosynthesized in situ by HeLa cancer cells treated with a specific silver salt derivative [Ag (GSH)]⁺ and exogenous GSH. Recently, the same group [38] explored the preparation of an intracellular temperature nanoprobe specifically by in situ biosynthesized fluorescent CuNCs in target cancer cells upon incubation with a special copper precursor (i.e., the complex solution of GSH and copper(II)). These fluorescent CuNCs could be biosynthesized spontaneously in MDA-MB-231 cancer cells through a particular molecular process, but not in normal cells (i.e., L02

cells). In a recent study, they demonstrated that fluorescent ZnO nanoclusters and magnetic Fe₃O₄ nanoclusters can also be synthesized in cancer cells [39].

Using GSH as a scaffold and sulfur–hydrazine hydrate complex (S–N₂H₄·H₂O) as the S²⁻ source, Wang et al. [40] developed a one-step approach to prepare water-soluble fluorescent Ag₂S NCs with tunable PL properties. By adjusting the amount of GSH and the ratio of Ag⁺ to S–N₂H₄·H₂O, Ag₂S NCs with different PL wavelengths and sizes were obtained. Subsequently, Xian group [41] successfully synthesized NIR-emitting fluorescence Ag₂S QDs in aqueous solution using 3-mercaptopropionic acid (3-MPA) as sulfur source and stabilizer. Interestingly, the fluorescence intensity of Ag₂S QDs was obviously enhanced upon the addition of various rare earth ions, especially in the presence of Gd³⁺. They speculated that the electrostatic interaction and coordination between rare earth ions and –COOH from MPA on Ag₂S QDs results in QDs aggregation and displays the feature of aggregation-induced emission (AIE).

Wang and coworkers [42] used a galvanic replacement reaction to prepare AgAu alloy NCs. In the first step, the template (i.e., AgNCs) was prepared by using GSH as the stabilizing agent and N₂H₄·2H₂O as the reducing agent. Then, when the AuCl₄⁻ ion and GSH were added to the aqueous solution of AgNCs, the galvanic replacement reaction occurred due to higher standard reduction potential of AuCl₄⁻/Au pair (0.99 V vs SHE) than that of Ag⁺/Ag pair (0.80 V vs SHE) [43]. The as-prepared AgAu alloy NCs displayed NIR fluorescence centered at 716 nm and showed tunable luminescence from visible red (614 nm) to NIR (716 nm) by controlling the Ag/Au ratios.

In addition to GSH, bidentate dihydrolipoic acid (DHLA) is another attractive ligand for MNCs synthesis due to its strong binding affinity to metal atoms. Shang et al. [11] synthesized NIR-emitting DHLA–AuNCs with a one-pot strategy by simply reducing a mixture of lipoic acid (LA) and gold salt with NaBH₄ in aqueous solution. The obtained AuNCs possess NIR emission and long fluorescence lifetime (>100 ns), making them attractive as markers for cellular

FLIM applications. Afterwards, the same group developed a microwave-assisted strategy for synthesizing DHLA–AuNCs [44]. Particularly, irradiation with microwaves during the synthesis enhanced the fluorescence QY of AuNCs by about fivefold from ~0.6% to 2.9%, and it also shortened the reaction time from hours to several minutes. Moreover, by using microwave irradiation, the emission peak red shifts from 690 nm to 715 nm upon excitation at 580 nm. Later, via a slightly modified strategy, Nair et al. [45] reported the synthesis of NIR-emitting (Au)₁₈(LA)₁₄ NCs with a higher QY, 10%. Besides AuNCs, Ghosh and coworkers [46] reported the synthesis of brightly red fluorescent DHLA–CuNCs, in combination with biocompatible polymer poly(vinylpyrrolidone) (PVP) as stabilizers. The fluorescence of CuNCs was found to be pH sensitive, and the emission could be tuned reversibly according to the pH.

Besides GSH and DHLA, other thiols such as tiopronin and mercaptosuccinic acid (MSA) have also been used as stabilizers, which yielded AuNCs centered at 785 nm with QYs in the range of 3–4% [47]. Recently, Zhou et al. [48] synthesized hydrophobicity-guided self-assembled particles of AgNCs with AIE (Fig. 1). They adopted a hydrophobic ligand, thiosalicylic acid, as capping agent to prepare AgNCs which showed significant AIE behavior. This AIE property of AgNCs enables them to sensitively respond to multiple external stimuli such as solvent polarity, pH, and environmental temperature. The hydrophobic nature of thiosalicylic acid as the capping ligand of AgNCs drives the formation of self-assembled particles of AgNCs with bright luminescence.

In addition to the above-mentioned strategy by direct reduction of metal ions in the presence of thiols, fluorescent MNCs can also be prepared by etching large metal nanoparticles with thiols. Au₂₃(SG)₁₈ NCs (SG denotes GSH) were obtained via the interfacial etching process using Au₂₅SG₁₈ NCs as the precursor. For interfacial etching, an interface was created by making an immiscible biphasic mixture of toluene containing octanethiol (OT) and an aqueous solution of Au₂₅SG₁₈. A highly fluorescent, water-soluble Au₂₃(SG)₁₈ cluster was obtained by etching at 25 °C

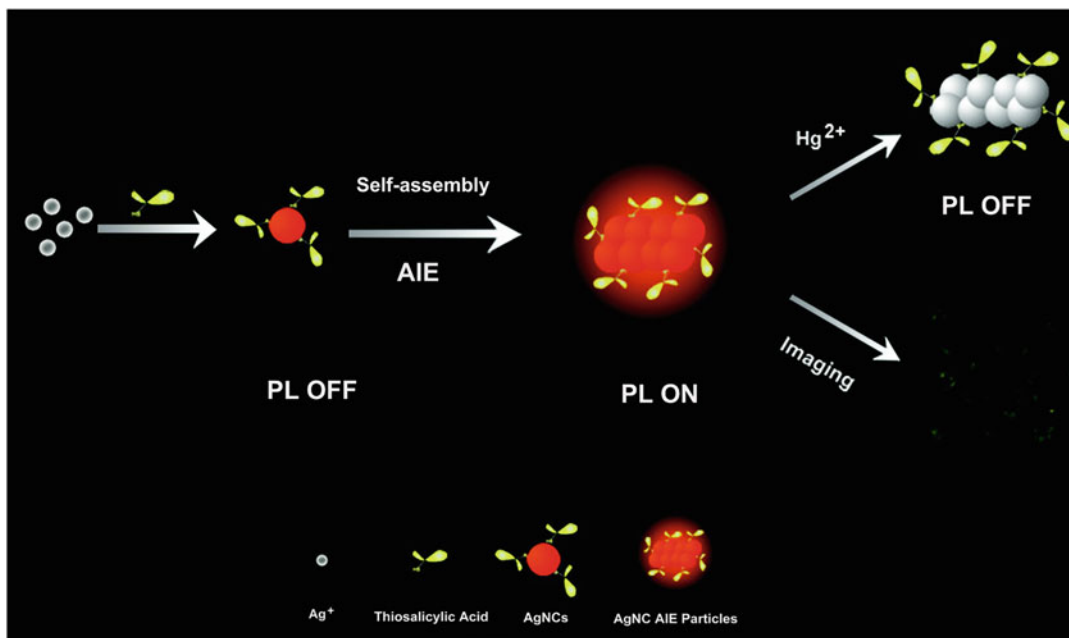


Fig. 1 Schematic of the fabrication of self-assembled particles of AgNCs with AIE and their use in quantifying mercuric ion and imaging cells. Reprinted with permission from Ref. [48]

[49]. Red-emitting AgNCs were produced by an interfacial etching route using GSH as a ligand etchant from MSA-protected AgNPs. These AgNCs show high photostability over time and a high stability for a wide pH range [50]. Lin and coworkers [51] developed a strategy to synthesize DHLA–AuNCs based on precursor-induced AuNPs etching in organic phase and ligand exchange with DHLA to transfer the particles into aqueous solution. Subsequently, the same group adopted a further 24 h thermal treatment at 70 °C to markedly increase the QY of AuNCs to nearly 7% [52].

2.2 Proteins, Peptides, and DNA Oligonucleotides

Biomacromolecules such as proteins and peptides have also been extensively utilized as templates for synthesizing fluorescent MNCs. Particularly, proteins possess abundant binding sites that can potentially bind and further reduce metal ions, thus offering promising scaffolds for template-

driven formation of small MNCs [53, 54]. Notably, bovine serum albumin (BSA) was first reported by Xie et al. as an excellent scaffold for AuNCs due to the strong force of Au–S bonding and the steric protection (Fig. 2), where NIR-emitting AuNCs with maximum emission wavelength at about 640 nm can be obtained [55]. Recently, Yu et al. [56] reported a kind of novel hybrid membrane made with AuNC-embedded BSA (AuNCs@BSA) fibrils and activated graphene oxide (GO), which was used to remove heavy metal ions, Hg^{2+} , from water. Later, researchers also tried many other proteins, such as transferrin-family proteins [57–59], trypsin [60], insulin [61], and ribonuclease A [62], as potential bioscaffolds for synthesizing MNCs. For example, transferrin (Tf)-templated CuNCs have been synthesized at room temperature via a biomineralization process, where ascorbic acid was used as the reductant. The as-prepared Tf-CuNCs exhibited intense NIR fluorescence with a QY about 6.2% [63]. Using denatured lysozyme (dLys) as the capping agent, a ratiometric fluorescent AgNCs probe was

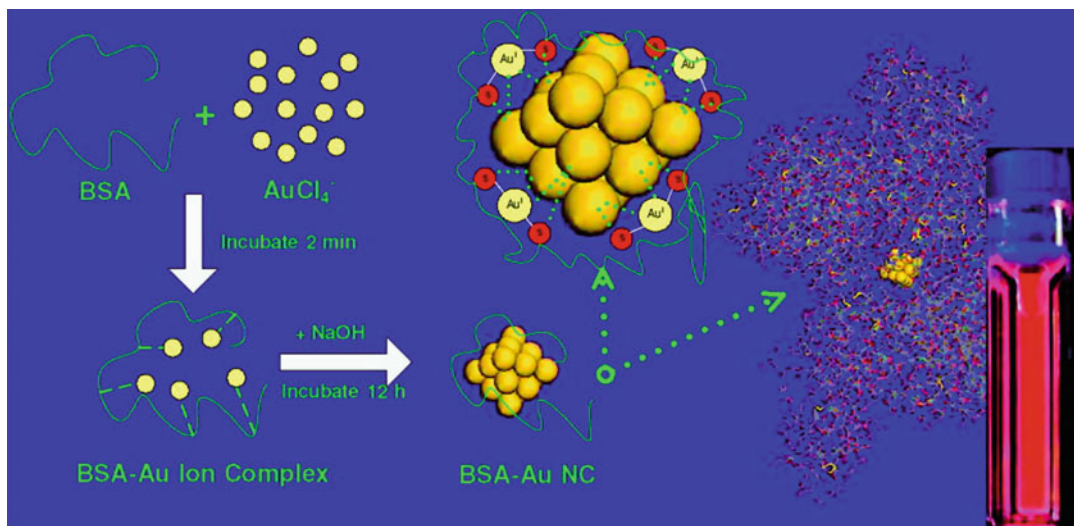


Fig. 2 Schematic of the formation of AuNCs in BSA solution under alkaline conditions. Reprinted with permission from Ref. [55]

developed [64]. This probe could be utilized for ratiometric detection of H₂O₂ and further exploited to H₂O₂-generated oxidase-based biosensing, such as glucose and acetylcholine chloride. Also, dual channel fluorescence confocal images of •OH in living cells was realized using the dLys-AgNCs probe. Besides their well-known roles as capping agents, proteins such as BSA can also function as etching agents for synthesizing fluorescent AuNCs in a few cases. For example, Pradeep et al. [65] employed a core etching method to synthesize BSA-AuNCs from MSA-capped AuNPs.

In addition to proteins, the integration of MNCs with peptides can also combine the distinct optical properties of MNCs with the biological functions of peptides [66, 67]. For example, Gao group [68] developed a one-step biomineralization method to produce AuNCs by using a bifunctional CCYTAT peptide, which contains one domain for biomineralizing and capturing AuNCs and another domain for targeting cell nuclei. The as-prepared AuNCs showed a maximum emission at 677 nm and possessed a high fluorescence QY of about 11%. Recently, by combining biomineralization and supramolecular self-assembly of motif-designed peptide constructs, researchers reported that the emission

of peptide-AuNCs can be enhanced by nearly 70-fold, which largely increases their utility for biological applications [69].

DNA have been employed in the design and fabrication of various DNA-templated metal nanostructures owing to their distinct interactions with metal cations [70]. In 2008, Dickson group [71] first reported the use of ssDNA to synthesize AgNCs with fluorescence tunable throughout the visible and NIR range. Notably, these AgNCs possessed a high QY up to 34%. Sharma et al. [72] also reported four different DNA sequences as AgNC templates with emission at different wavelengths. The resulting NIR-emitting AgNCs had QY greater than 50% and were very promising as biolabels. It has been shown in earlier reports that Ag⁺ has a higher binding affinity to cytosine bases than other bases [73–75]. Therefore, Dickson and coworkers [76, 77] reported NIR-emitting AgNCs creating in single-stranded oligo-DNA consisting of 12 or 24 cytosine bases. By using more advanced DNA structures, such as G-quadruplex, as the template, Wang group [78] reported the synthesis of fluorescent AgNCs made of 2–4 Ag atoms centered at 680 nm. Furthermore, intrinsically fluorescent AgNCs–aptamer assemblies for cell recognition were developed by Wang and coworkers

[79]. They employed a cancer-targeted DNA aptamer sequence (A-strand) and cytosine-rich sequence for templated synthesis of fluorescent AgNCs (C-strand). A fluorescent sgc8c-AgNCs assembly with relatively high luminescence has been achieved and exhibited specific binding to target CCRF-CEM cells by using a six-base adenine linker. Subsequently, adopting a similar method, the same group [80] reported a label-free and turn-on aptamer strategy for cancer cell detection based on the recognition-induced conformation alteration of aptamer and hybridization-induced fluorescence enhancement effect of DNA-AgNCs in proximity of guanine-rich DNA sequences (Fig. 3). In this strategy, two tailored DNA probes were designed, namely, a recognition probe (R-Probe) and a signal probe (S-Probe). In the presence of target cancer cells, recognizing and binding of the aptamer to the protein receptors on the cancer cells surface enforces the R-Probe to undergo a conformational alteration, causing the arm segment dissociation. The hybridization between the arm segment in the R-Probe and the link sequence in the S-Probe could then be initiated. Finally, the S-Probe-templated dark AgNCs are brought close to the guanine-rich DNA sequences and changed to bright AgNCs, leading to enhanced fluorescence readout.

2.3 Polymers

There are also efforts on using polymer as stabilizers for preparing fluorescent MNCs based on their capability of sequestering metal ions from solutions. Moreover, the terminal groups on the polymer periphery are very useful for the further bioconjugation of MNCs. For instance, Huang and coworkers [81] prepared NIR-emitting AuNCs by using multidentate polymer, thioether-terminated poly(methacrylic acid) (PTMP-PMAA), as ligands. In another report, fluorescent poly(ethylene glycol) (PEG)-AuNPs with an emission peak at 810 nm were created by thermally reducing HAuCl₄ in the presence of thiolated PEG ligands with a molecular weight (MW) of 1 kDa in aqueous solution

[82]. Similarly, Wang et al. [83] reported a one-pot fabrication of thiol-terminated polyethyleneimine (SH-PEI) stabilized NIR-emitting AgNCs. SH-PEI not only acts as an excellent stabilizer for AgNCs but also facilitates post-surface modification with functional biomolecules. Inouye and coworkers [84] synthesized Pt₅(MAA)₈ NCs with an 18% QY in water. Upon bioconjugating an antibody, they successfully labeled chemokine receptors in living HeLa cells. Afterwards, the same group investigated the formation of yellow fluorescent PEI-protected PtNCs (PtNCs@PEI) [85]. They found that PtNCs were produced in the cavities formed by coiled PEI ligands and were mostly stabilized with the amino groups (-NH₂). The size and fluorescence properties of PtNCs@PEI are strongly related to the cavities formed by the coiled PEI ligands. As shown in Fig. 4, under alkaline pH conditions, PEI have the ability to coil around the surface of PtNCs to form the cavities. As for the neutral condition (all primary amines protonated), the hydrodynamic size of PtNCs is a little larger than ones produced under basic condition, resulting in the slight shift to longer emission wavelength. At acidic pH (most amines protonated), both PEI and PEI-capped NCs possess considerable positive charges, leading to an expansion of PEI chains because of the repulsion between the charged amines. The dimension of cavity in the acidic situation is much bigger than that in the basic situation, caused the larger PtNPs and no emitted fluorescence.

Recently, poly(amidoamine) (PAMAM) dendrimer-hosted Au₅NCs were successfully synthesized through a two-stage growth process with a high fluorescence QY up to 25% [86]. As shown in Fig. 5, stage I presented a simultaneous self-nucleation of Au₅NCs and subsequent PAMAM-hosted self-assembly with a rapid rate of fluorescence increase. At stage II, the fluorescence enhancement should be mainly dominated by the self-assembly of Au₅NCs in PAMAM matrix. First, the emission from self-assembled aggregates was attributed to ligand-to-metal-metal charge transfer (LMMCT) from electron-rich-NH₂ groups in PAMAM to Au atoms, which

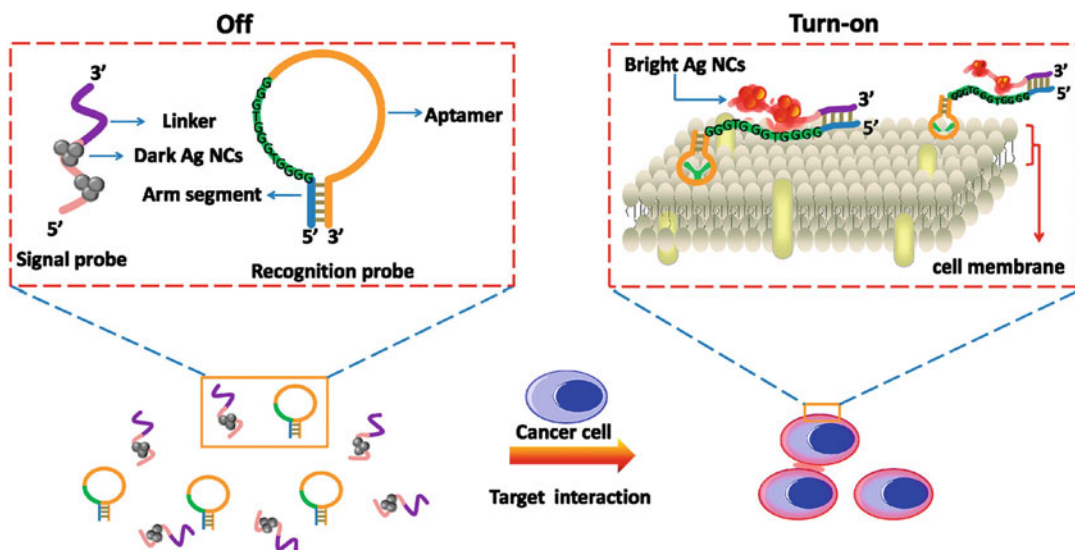


Fig. 3 Schematic representation of the label-free and turn-on aptamer strategy for cancer cell detection based on DNA-AgNCs fluorescence upon recognition-induced hybridization. Reprinted with permission from Ref. [80]

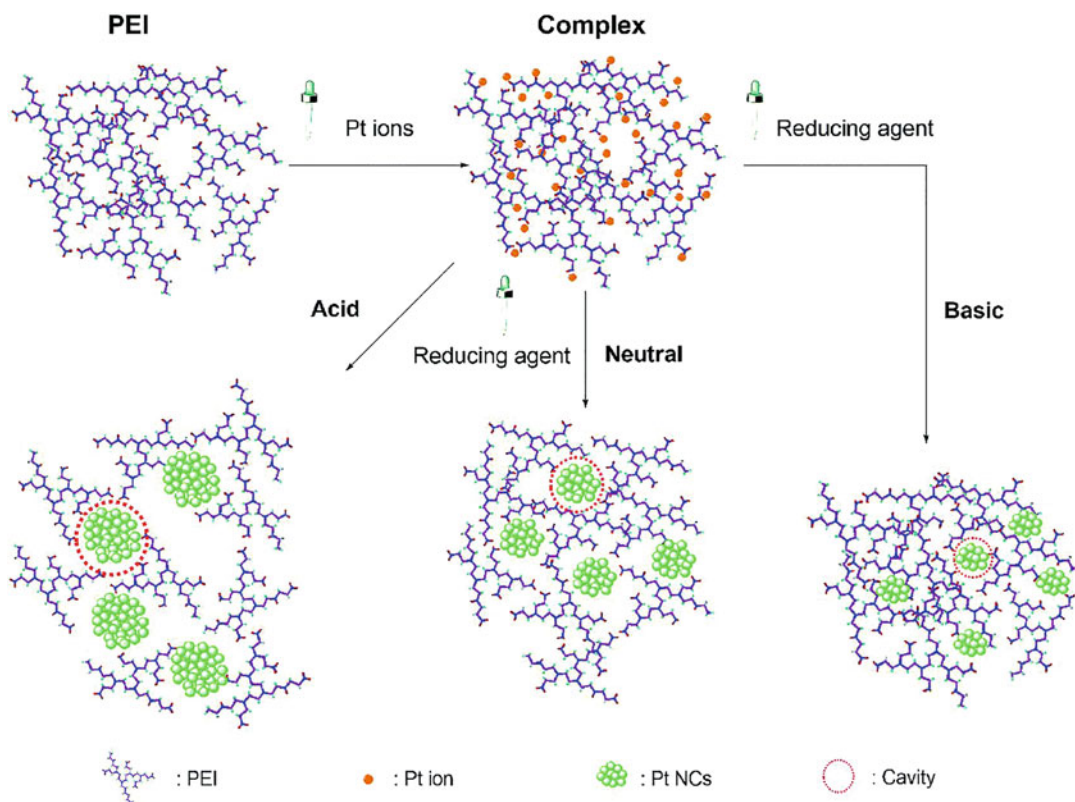


Fig. 4 Schematic formation of PEI chelation with Pt ions and reduced PtNCs in PEI cavities at different pH mediums. Reprinted with permission from Ref. [85]

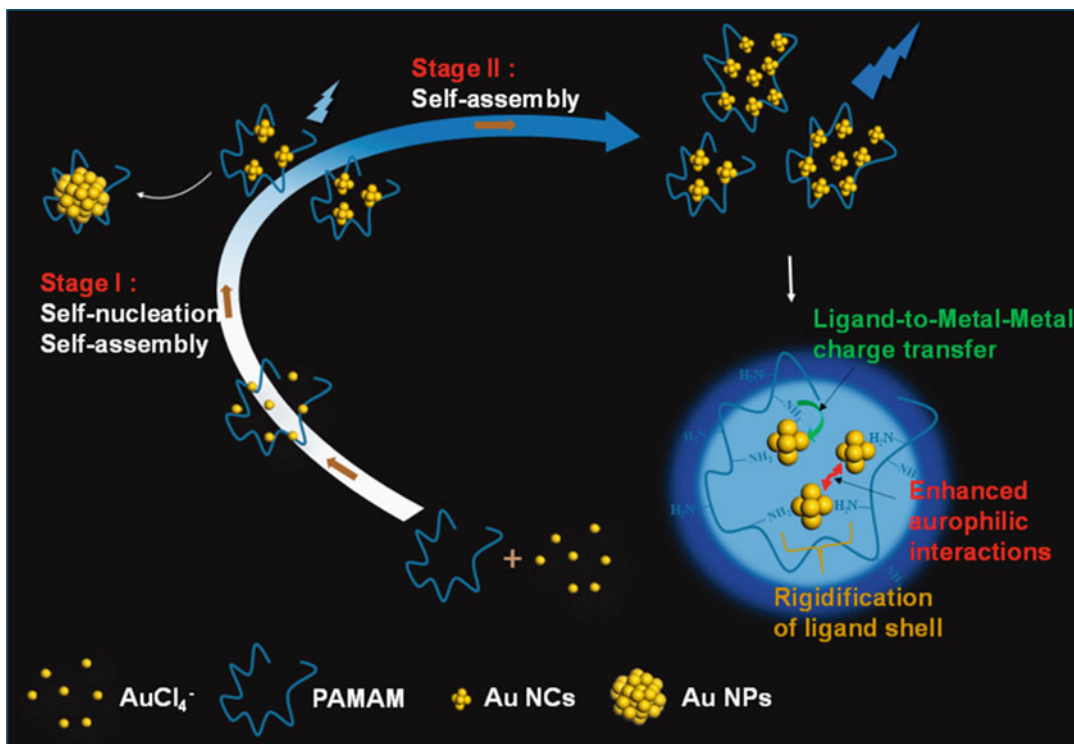


Fig. 5 Schematic illustration of growth process and the structure of Au₅NCs self-assemblies in PAMAM matrix. Reprinted with permission from Ref. [86]

generated radiative relaxation through a metal-centered triplet state. In addition, because PAMAM endowed AuNCs with stronger inner interactions compared to those isolated species, enhanced aurophilic interactions greatly promote excited-state relaxation dynamics and enhanced rigid structures reduced the level of nonradiative relaxation of excited states, which was also responsible for enhanced emission [87].

3 MNCs for Fluorescence Bioimaging

With many attractive features including ultra-small size, good biocompatibility, brightness, and photostability, MNCs are promising fluorescence probes for biological imaging. Indeed, great progress has been achieved in recent years on employing fluorescent MNCs for biological imaging applications, as summarized in Table 2.

In 2012, Shang et al. [44] demonstrated the utilization of DHLA–AuNCs for imaging intracellular Hg²⁺ in living HeLa cells, where they observed the intracellular fluorescence quenching effect upon addition of Hg²⁺ ions. Subsequently, the same group [94] systematically investigated the interactions of AgNCs with human serum albumin (HSA). They found that protein adsorption markedly changes the uptake behavior as well the cytotoxicity of AgNCs. The amount of AgNCs internalized by the cells is substantially reduced in the presence of HSA. Moreover, the fluorescence from intracellular AgNCs is stronger than that from membrane-associated particles in both cases, the fluorescence decrease in the membrane region (ca. 13-fold) is much larger than for inside the cells (ca. sevenfold). Afterwards, they systematically varied the surface charge of HSA to examine the effect of Coulomb forces in modulating the biological interactions of AuNCs [116]. By utilizing confocal fluorescence

Table 2 Fluorescent MNCs as single-modal fluorescence imaging probes

Metal	Capping agent	Functionalization	λ_{em} (nm)	Imaging modal	Biosystems	Ref.
Au	DHLA	–	715	Intensity	HeLa cells	[44]
Au	DHLA	–	684	Intensity	HeLa cells	[116]
Au	CCYTAT	–	677	Intensity	HeLa cells	[68]
Ag	G-quadruplex (AS1411)	–	680	Intensity	HeLa cells	[78]
Ag	GSH	–	645	Intensity	HeLa cells	[34]
Ag	DHLA	–	630	Intensity	HeLa cells	[94]
AuAg	LA	–	630	Intensity	HeLa cells	[91]
Cu	Lysozyme	–	450	Intensity	HeLa cells	[109]
Cu	Transferrin	–	670	Intensity	HeLa cells	[63]
Cu	DHLA	–	650	Intensity	HeLa cells	[46]
Cu	GSH	–	585	Intensity	HeLa cells	[89]
Cu	GSH	–	430	Intensity	HeLa, MDAMB-231, A549 cells	[88]
Cu	GSH	–	610	Intensity	MC3T3-E1 cells	[35]
Cu	GSH	–	610	Intensity	MDA-MB-231 cancer cells	[38]
Cu	TA	–	430	Intensity	A549 cells	[95]
Mg	BSA	–	465	Intensity	A549 cells	[106]
Au	Human transferrin	–	695	Intensity	A549 lung tumor cells	[59]
Au	PTMP-PMAA	–	~660	Intensity	Hematopoietic cancer cells K562	[81]
Ag	GSH	–	720	Intensity	Epithelial lung cancer cells (A549)	[50]
Ag	GSH	–	640	Intensity	Lung cancer cells (A549)	[31]
Ag	TSA	–	612	Intensity	Human A549 cells	[48]
Ag	dLys	–	640	Intensity	PC-3 cells	[64]
Ag	Sodium cholate	–	406, 430	Intensity	Zebrafish embryos	[100]
Ag	DNA	–	550	Intensity	CCRF-CEM cancer cells	[80]
Ag	DNA (AS1411)	–	635	Intensity	MCF-7 human breast cancer cells	[112]
Ag ₂ S	GSH	–	679	Intensity	MC3T3-EI cells	[40]
Ag ₂ S	3-MPA	–	795	Intensity	MDA-MB-468 cells	[41]
AuAg	GSH	–	716	Intensity	CAL-27 cells	[42]
AuAg	PEI-LA	–	680	Intensity	B16F10, HeLa, and CHO cells, BALB/C nude mice	[92]
AuCe	GSH	–	570	Intensity	HeLa cells, cervical carcinoma tumor xenograft mice	[90]
AuCe	BSA	–	650	Intensity	HeLa cells	[127]
Au	BSA	–	710	Intensity	MDA-MB-45 tumor and HeLa tumor xenograft mice	[101]
Au	Apo ferritin	–	665	Intensity	Human Caco-2 cells, nude mice	[58]
Au	GSH	–	810	Intensity	MCF-7 tumor-bearing mice	[29]
Au	PEG	–	810	Intensity	MCF-7 tumor-bearing mice	[82]
Ag	GSH	–	670	Intensity	HeLa cells, tumor-bearing mice	[37]
Au	Human insulin	–	680	Intensity	Chondrocytes, mice	[61]
Au	BSA	FA	~674	Intensity	Oral carcinoma KB cells	[104]
Au	BSA	FA	660	Intensity	Oral carcinoma KB cells	[65]
Au	BSA	FA	665	Intensity	FR-positive tumor cells, tumor-bearing mice	[102]
Au	BSA	FA	655	Intensity	MCF-7 cells, MCF-7 xenograft tumors	[140]

(continued)

Table 2 (continued)

Metal	Capping agent	Functionalization	λ_{em} (nm)	Imaging modal	Biosystems	Ref.
Au	Ovalbumin	FA	626	Intensity	HeLa cells	[141]
Au	GSH	FA	642	Intensity	HeLa and KB cells	[142]
Au	LA	FA	720	Intensity	C6 rat glial cancer cells, subcutaneous C6 glial tumor mouse	[45]
Au	Trypsin	FA	690	Intensity	HeLa tumor-bearing mice	[60]
Ag	MT	FA	632	Intensity	HeLa cells	[99]
Ag	SH-PEI	FA	690	Intensity	MCF-7 cells; tumor-bearing mice	[83]
Cd	BSA	HA	475	Intensity	MCF-7 breast cancer cells	[105]
Au	GSH	Streptavidin	685	Intensity	Human hepatoma cells (HepG2)	[49]
Au	DHLA	Streptavidin	650	Intensity	Human hepatoma cells (HepG2)	[51]
Au	Bovine pancreatic ribonuclease A	Vitamin B ₁₂	682	Intensity	Human Caco-2 cells	[62]
Au	BSA	SiO ₂	670	Intensity	Lung tumor cells	[103]
Au	GSH	SiO ₂	565	Intensity	HeLa cells	[126]
Au	Chitosan	TPP	440	Intensity	HeLa cells	[124]
Au	N-acetyl-L-cysteine	Chitosan	680	Intensity	HeLa cells	[122]
Pt	MAA	Anti-CXCR4-Ab antibody	470	Intensity	HeLa cells	[84]
Pt	PEI	Anti-CXCR4-Ab antibody	560	Intensity	HeLa cells	[85]
Ag	ssDNA	SWCNTs	620	Intensity	HeLa cells	[143]
Ag	DNA	Aptamer	595	Intensity	HeLa cells	[144]
Au	BSA	Met	655	Intensity	Met receptor positive tumor cells, tumor-bearing mice	[120]
Au	BSA	GSH	660	Intensity	4T1 breast cancer cells, 4T1 tumor-bearing mice	[121]
Au	Human transferrin	GO	710	Intensity	HeLa cells, HeLa tumor-bearing mice	[57]
Au	DHLA	Liposome	650	Intensity	Human endothelial cells, hindlimb ischemic mice	[52]
Cu	BSA	LHRH peptide	~410	PET	Orthotopic A549 lung tumor-bearing mice	[131]
⁶⁴ CuAu	GSH	–	800	PET	BALB/c mice	[145]
⁶⁴ CuAu	TA-PEG	Plerixafor	–	PET	4T1 tumor-bearing mice	[133]
Au	DHLA	–	684	FLIM	HeLa cells	[11]
Au	MSA/tiopronin	PEG	785	FLIM	HeLa cells	[47]
Au	LA	–	715	FLIM	HeLa cells	[136]
Au	BSA	Herceptin	640	FLIM	SK-BR3 cells	[137]
Ag	HSA, BSA	GO	620, 510	FLIM	K562 cells	[107]
Au	11-MUA	Dextran	530	Two-photon	Human mesenchymal stem cells (hMSCs)	[96]
Au	GSH	–	780	Two-photon	SH-SY5Y human neuroblastoma cells	[28]
Au	DPA	–	610	Two-photon	HeLa cells	[98]
Au	BSA	DOX	655	Two-photon	HeLa cells	[138]

(continued)

Table 2 (continued)

Metal	Capping agent	Functionalization	λ_{em} (nm)	Imaging modal	Biosystems	Ref.
Au	BSA	RGD	650	Two-photon	U87-MG cancer cells	[139]
Cu	Peptide	–	460	Two-photon	HeLa cells, A549 cells	[108]

DHLA dihydrolipoic acid, *LA* lipoic acid, *CCYTAT* H₂N–CCYGRKKRRRQRRR–COOH, *TA* tannic acid, *PTMP* pentaerythritol tetrakis 3-mercaptopropionate, *PMAA* poly(methacrylic acid), *GSH* glutathione, *PEG* poly(ethylene glycol), *TSA* thiosalicylic acid, *dLys* denatured lysozyme, *BSA* bovine serum albumin, *FA* folic acid, *PEI* polyethyleneimine, *LA* lipoic acid, *MT* metallothionein, *SH-PEI* thiol-polyethyleneimine, *HA* hyaluronic acid, *TPP* triphenylphosphonium, *MAA* mercaptoacetic acid, *PEI* polyethyleneimine, *SWCNTs* single-walled carbon nanotubes; *Met* methionine, *GO* graphene oxide, *PET* positron emission tomography, *LHRH* luteinizing hormone releasing hormone, *TA-PEG* thioctic acid–polyethylene glycol, *MSA* 2-mercaptosuccinic acid, *tiopronin* N-(2-mercapto-propionyl) glycine, *FLIM* fluorescence lifetime imaging, *11-MUA* 11-mercaptopundecanoic acid, *DPA* D-penicillamine, *DOX* doxorubicin

microscopy to observe the uptake and localization of AuNCs in HeLa cells, they found distinct difference in the cellular uptake of AuNCs adsorbed with differently modified HSA (Fig. 6): nHSA (native HSA) suppressed cellular uptake, aHSA (HSA with more negative surface charges) showed negligible effect, and cHSA (HSA with more positive surface charges) enhanced cellular uptake. The results provide helpful information in designing NIR AuNCs aiming to highly efficient cell labeling applications.

Gao and coworkers [68] found that peptide–AuNCs with a bifunctional CCYTAT peptide could specifically target the nucleus of three different cell lines, including normal cells human gastric mucosa cells (GES-1), human embryonic lung fibroblast cells (MRC-5), and human cervical cancer cells (HeLa). Ai et al. [78] successfully employed G-quadruplex AS1411-templated AgNCs for specific bioimaging HeLa cells. Besides, Guével et al. [50] employed GSH-AgNCs as optical probes for NIR fluorescence imaging of epithelial lung cancer A549 cells. Confocal images showed that AgNCs were taken up in the cytoplasm and more specifically in the vesicles of A549 cells, but were absent in the nucleus. In contrast, Wang and coworkers [40, 42] observed that GSH-capped Ag₂S NCs and AgAu alloy NCs were distributed in both cytoplasm and the cellular nucleus of MC3T3-E1 cells and CAL-27 cells. These differences in the intracellular localization of MNCs upon the internalization suggest that not only the surface

ligands but also the cell types can influence their intracellular fate.

A large number of reports have also focused on tumor imaging in vivo currently. For example, Wu et al. [101] reported the first example of tumor imaging with BSA-AuNCs. Their in vivo tumor targeting and ex vivo imaging studies showed that these ultrasmall AuNCs were highly accumulated in the tumor areas (Fig. 7) due to the enhanced permeability and retention (EPR) effects. Sun and coworkers [58] achieved ferritin receptor-mediated targeting and bioimaging with far-red emitting paired AuNCs. These far-red luminescent AuNCs could act as an excellent probe for targeting ferritin receptor-overexpressed human Caco-2 cells and whole female nude mice body imaging with specific targeting to the kidney. In addition, renal-clearable NIR-emitting GSH-AuNCs and PEG-AuNCs have been reported for in vivo NIR tumor targeting of MCF-7 tumor-bearing mice [29, 82]. They not only exhibited efficient renal clearance and low reticuloendothelial system (RES) accumulation but also showed a much longer tumor retention time and faster normal tissue clearance.

Furthermore, Wang et al. [37] reported the use of biosynthesized NIR-emitting AgNCs for in situ imaging cancer cells and tumors, which did not occur in normal cells and tissues. The same group also explored the possibility of imaging cancer cells through in situ self-biosynthesized ZnNCs [117]. Particularly, in vivo imaging of

Fig. 6 Three-dimensional fluorescence confocal images of HeLa cells upon incubation with AuNCs (2.5 μ M, green) for 2 h: (a) without proteins and with 2.5 μ M (b) nHSA, (c) aHSA, and (d) cHSA. Cell membranes were stained with CellMask DeepRed (red). The data are shown as sections in the x-y plane (upper left), x-z plane (lower left), and y-z plane (right). Scale bar, 10 μ m. Reprinted with permission from Ref. [116]

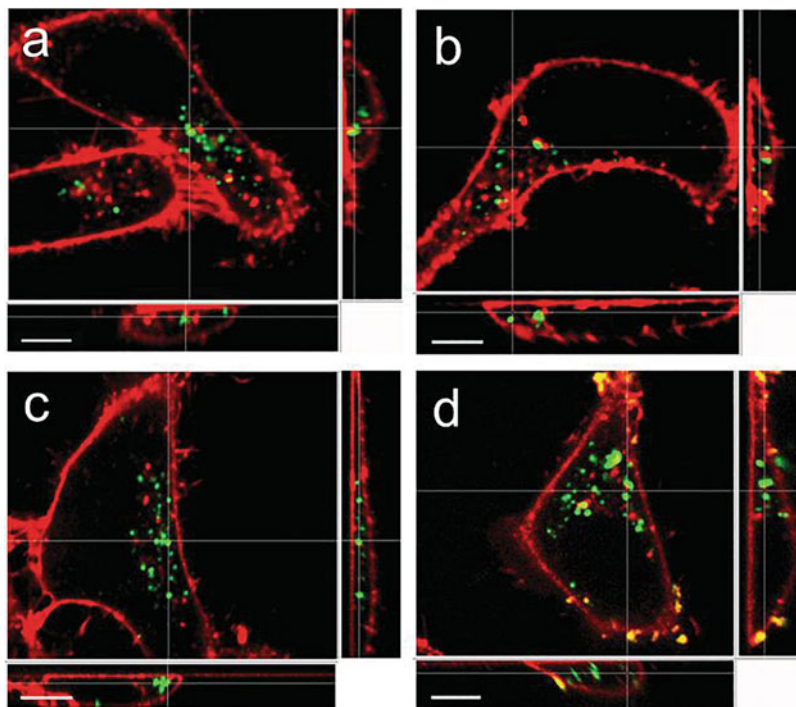
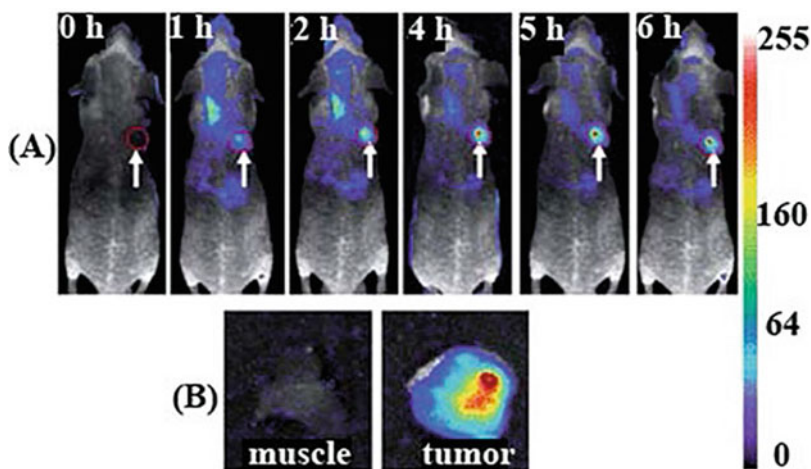


Fig. 7 (a) Fluorescence images of mice bearing an MDA-MB-45 tumor. Strong signal from AuNCs was observed in the tumor (marked by the red circle). The arrowheads indicated the tumor. (b) Ex vivo fluorescence image of the tumor tissue and the muscle tissue around the tumor from the mice used in A. Reprinted with permission from Ref. [101]



subcutaneous xenografted tumors in nude mice has also established the validity of this strategy for the rapid and precise target self-bioimaging of tumors by subcutaneous injections of zinc gluconate solutions, without significant dissemination to the surrounding normal tissues. Recently, they explored a facile and green strategy to in situ

biosynthesize fluorescent CuNCs in cancer cells [38]. As shown in Fig. 8, it is evident that fluorescent CuNCs could be spontaneously biosynthesized in cancer cells for intracellular fluorescence imaging, which could not be biosynthesized in normal cells. More importantly, the relevant fluorescence intensity of the in situ

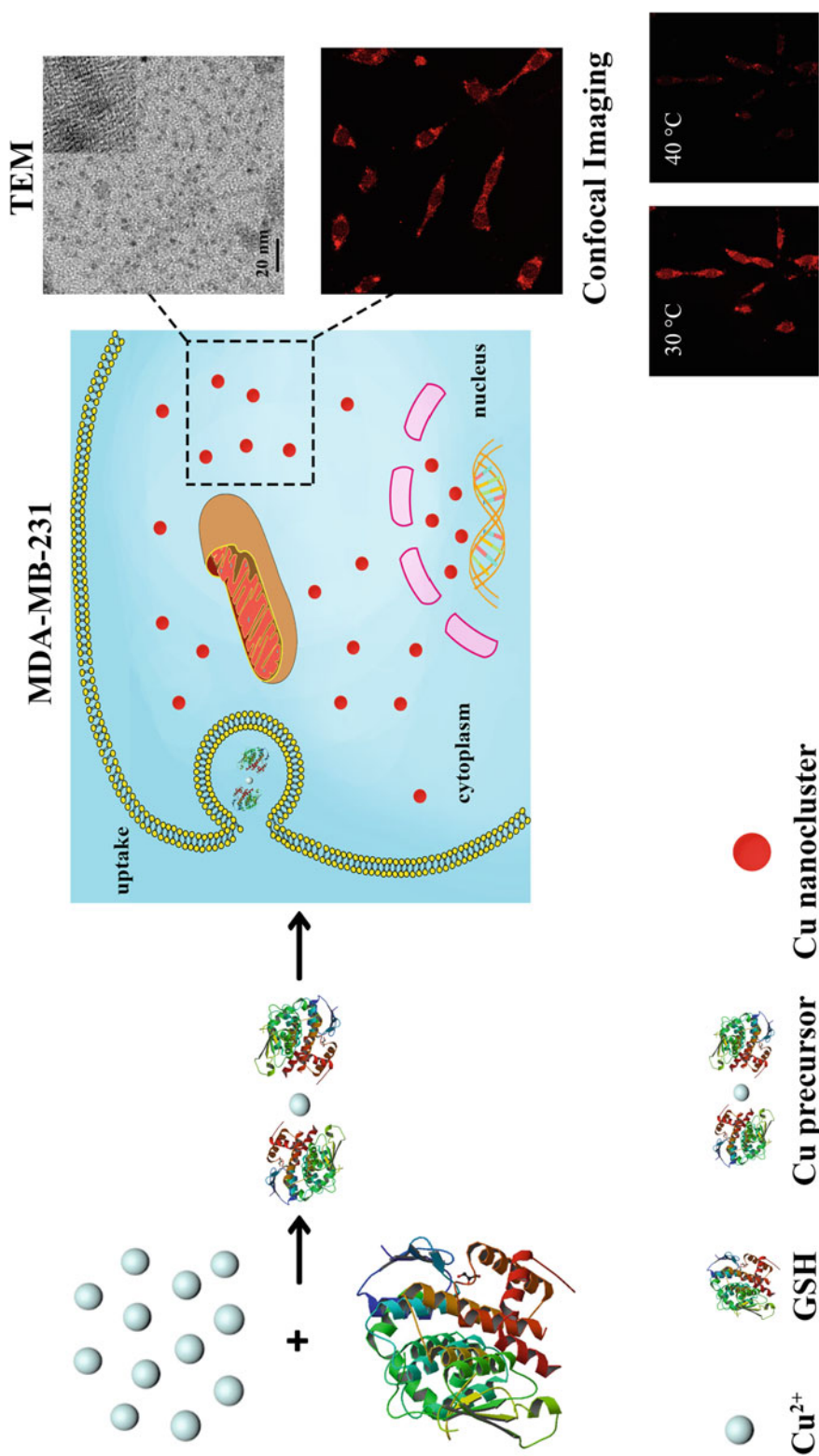


Fig. 8 Schematic illustration of the process for the spontaneous biosynthesis of fluorescent CuNCs in cancer cells for intracellular fluorescence imaging and temperature measurement. Reprinted with permission from Ref. [38]

biosynthesized CuNCs was reversibly and sensitively responsive to physiological temperature changes in MDA-MB-231 cancer cells. Besides, Liu et al. [61] successfully synthesized fluorescent human insulin–Au nanodots (NDs) for *in vivo* imaging of insulin metabolism. Investigations on mice ear and *ex vivo* assays on human fat tissues showed that cells with rich insulin receptors had higher uptake of administrated insulin.

For targeted imaging of cancer cells and tumors, MNCs are modified with specific recognition units such as folic acid (FA) and streptavidin. For example, targeted imaging of folate receptor (FR) positive oral carcinoma KB cells using FA-conjugated BSA–AuNCs has been reported [65, 104]. Tumor targeting and specific affinity of FA-conjugated AuNCs for FR over-expressed tumors facilitated the accumulation of AuNCs in the tumor site, which enhanced the fluorescence signal in the tumor site, enabling *in vivo* targeted imaging of tumors with high specificity and also the subsequent tumor therapy [45, 60, 102]. Recently, Wang et al. [83] reported the conjugation of PEI–AgNCs with FA for both *in vitro* and *in vivo* targeted imaging. Their results indicated that the clearance rate of FA-conjugated AgNCs in the tumor-bearing mice was much slower than that in the normal mice because the high affinity of FA to target tumors inhibited FA–AgNCs from being metabolized. Moreover, Chen et al. [118] synthesized core–shell structured multifunctional nanocarriers for targeted anticancer drug delivery, where FA-conjugated amphiphilic hyperbranched block copolymer was used as shell on the surface of AuNCs. The nanocarriers specifically targeted cancer cells because of the enhanced cell uptake mediated by FA moiety. Similarly, the multifunctional anticancer drug paclitaxel (PTX)-loaded AuNCs/FA-modified poly(DBAM-*co*-NAS-*co*-HEMA) (PDNH) core-satellites nanocomposites were fabricated, which possessed simultaneous cancer imaging, targeted drug delivery, and controlled anticancer drug release [119]. *In vivo* studies showed the selective accumulation of FA-conjugated nanocomposites in tumor tissues, and the drug delivery process could be

continuously monitored by the imaging probes, AuNCs. Similarly, streptavidin-conjugated AuNCs have been reported to specifically label endogenous biotin within human hepatoma cells (HepG2) using the specific interactions between streptavidin and biotin [49, 51].

Apart from FA and streptavidin, other functionalized molecules have also been used to conjugate with MNCs. For instance, Kong et al. [62] developed a multifunctional nanoprobe for simultaneous targeting and imaging of human colon carcinoma Caco-2 cells by conjugating vitamin B₁₂ to the ribonuclease A-stabilized AuNCs. Chen et al. [120] fabricated a fluorescent nanoprobe capable of specifically targeting carcinoma cells and tumors by coupling methionine (Met) and an NIR organic fluorescent dye MPA to BSA–AuNCs (Au–Met–MPA). Cui et al. [121] synthesized well-defined AuNCs nanoassembly by the self-assembly of reduced AuNCs using GSH as linkers. The as-prepared nanoassembly displayed highly effective cellular uptake and precise tumor targeting for NIRFL imaging *in vivo* compared to that of individual AuNCs. Wang et al. [57] reported the fabrication of Tf–AuNCs/GO nanocomposite (Tf–AuNCs/GO) for turn-on NIR fluorescence bioimaging of transferrin receptor (TfR) over-expressed HeLa cells and HeLa tumor-bearing mice.

Duan et al. [122] applied chitosan grafted with N-acetyl-L-cysteine (NAC-CS) as the template to prepare NIR fluorescent AuNCs (AuNCs@NAC-CS), which possessed many advantages in cell imaging, such as low cytotoxicity, low sensitivity to tumor cells contents (H₂O₂ and protease), and long-time cell imaging. During *in vivo* experiments, the obvious fluorescence signal of AuNCs@NAC-CS appeared in the liver and kidney of the normal mice after 6 h injection. The ultrasmall NPs were efficiently cleared which overcomes the toxicity by nonspecific accumulation in healthy tissues/organs from renal *in vivo* [123]. Triphenylphosphonium (TPP), a kind of delocalized lipophilic cations capable of selectively accumulating into highly negatively charged mitochondria of living cells, has been employed in functionalizing chitosan–AuNC composites (AuNCs@CS-TPP) for targeted

mitochondrial imaging in living cells [124]. By functionalizing of TAT peptide on the surface of AuNCs, multifunctional TAT peptide–AuNCs are designed for simultaneous fluorescence imaging as well as NIR light activated nucleus-targeting photodynamic therapy [125]. Recently, by combining biomineralization and supramolecular self-assembly of motif-designed peptide constructs containing an RGD sequence, Su et al. [69] have demonstrated the utility of AuNC-incorporated peptide nanofibers for targeted imaging of cancer cells.

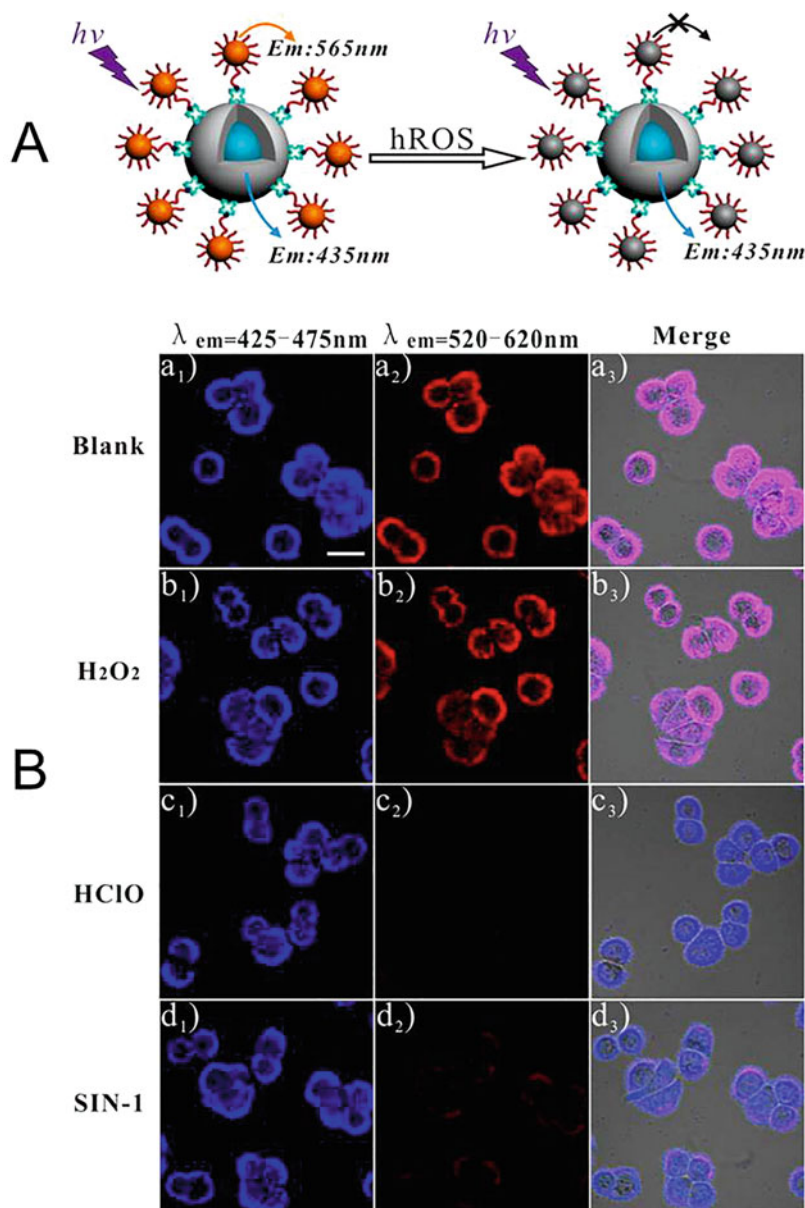
Taking advantage of their good cellular imaging properties, metal NC-based composites have been developed for real-time imaging of important physiological events in the intracellular environment. For instance, a novel nanocomposite has been developed through a crown-like assembly of dye-encapsulated silica particles decorated with satellite AuNCs for imaging of highly reactive oxygen species (hROS) in live cells [126]. This composite exhibits single-excitation and dual-emission fluorescent properties, one emission at 565 nm originating from the AuNCs, which fluorescence can be quenched substantially by hROS, and the other at 435 nm arising from the silica particles acting as an internal reference (Fig. 9a). When the composite-loaded cells were incubated with H₂O₂, a kind of weak ROS, strong fluorescence signals at both the blue and the red channels remained constant (Fig. 9b). However, a remarkable change was observed in the fluorescence images when the composite-loaded cells were incubated with hROS, such as HClO and ONOO⁻, 3-morpholinopyridone-imine (SIN-1) can slowly releases ONOO⁻. Chen et al. [127] reported a dual-emission BSA-templated (cerium) CeAuNCs probe for ratiometric determination of local pH values inside cells. Recently, Pan et al. [128] used viscosity-sensitive GSH-AuNCs with diffusion-dependent emission for viscosity imaging in live cells. Nystatin can induce mitochondrial malfunction by causing structural changes or swelling of mitochondria, resulting in a sharp increase of viscosity in the cells [129, 130]. A remarkable fluorescence enhancement effect can be

observed for the cells successively treated with nystatin and AuNCs.

Gao et al. [131] first developed ultrasmall chelator-free radioactive [⁶⁴Cu]CuNCs using BSA as a scaffold for PET imaging in an orthotopic lung cancer model. By preconjugating tumor target peptide luteinizing hormone releasing hormone (LHRH) to the BSA shell, the prepared [⁶⁴Cu]CuNC@BSA-LHRH showed high uptake in A549 human lung tumor, high radiolabeling stability, and rapid renal clearance characteristics. After injecting via tail vein into mice bearing orthotopic A549 lung tumors, the orthotopic A549 tumors of the left lung were clearly delineated with very little local background in the whole-body PET imaging of mice injected with [⁶⁴Cu]CuNC@BSA-LHRH (Fig. 10b). It is noticeable, however, that a significant difference in [⁶⁴Cu]CuNCs uptake between [⁶⁴Cu]CuNC@BSA and [⁶⁴Cu]CuNC@BSA-LHRH is observable after 0.5–4 h post-injection. The [⁶⁴Cu]CuNC@BSA-LHRH was retained preferentially in the orthotopic lung tumor by combined active targeting and passive targeting after injection [132]. Although [⁶⁴Cu]CuNC@BSA also showed partial tumor localization due to passive targeting by the effective EPR effect [132], most of the [⁶⁴Cu]CuNC@BSA distributed in the kidney and bladder (Fig. 10a). In another study, Liu and coworkers [133] prepared ⁶⁴Cu doped AuNCs (⁶⁴CuAuNCs) functionalized with AMD3100 (or Plerixafor) for targeted PET imaging of CXCR4, an up-regulated receptor on primary tumor and lung metastasis in a mouse 4 T1 orthotopic breast cancer model. In contrast to the ligand tracer alone (⁶⁴Cu–AMD3100) and NCs (⁶⁴CuAuNCs) without the conjugation of AMD3100, the targeted ⁶⁴CuAuNCs–AMD3100 exhibited higher sensitivity, better accuracy, and much earlier detection of CXCR4 expression in lung metastasis. Radionuclide ⁶⁴Cu-doped alloy ⁶⁴CuAuNCs have also be used as targeted probes for PET imaging in U87MG glioblastoma xenografted mice [134] and prostate cancer bearing mice [135].

FLIM is a powerful technique for cell imaging, which can take advantage of MNCs that typically

Fig. 9 (a) Schematic illustration of hROS detection using dye-encapsulated silica particles decorated with satellite AuNCs. (b) Confocal fluorescence microscopy images of HeLa cells after incubation with silica-AuNC composites for 1 h. Cells were (a) untreated or treated with (b) 1 mM H_2O_2 for 10 min, (c) 200 μM HClO for 5 min, and (d) 3 mM SIN-1 for 40 min. Reprinted with permission from Ref. [126]



possess longer fluorescence lifetime than the lifetime of the autofluorescence from cellular organelles, and thus they can easily be imaged by using lifetime gating. Upon FLIM imaging, the researchers observed that AuNCs located near the cell membrane displayed longer lifetimes than those internalized inside the cells [11], indicating that FLIM imaging not only reveals the cellular uptake of AuNCs but also provides information

on their different local environment. Later, based on the fact that the fluorescence intensity as well as the lifetime of DHLA-AuNCs is highly dependent on the temperature, Shang et al. [136] demonstrated the utilization of AuNC-based FLIM imaging for temperature sensing in live cells. As shown in Fig. 11, with increasing the temperature, the fluorescence lifetime decreased markedly from 970 ns at 14 °C to 670 ns at 43 °C,

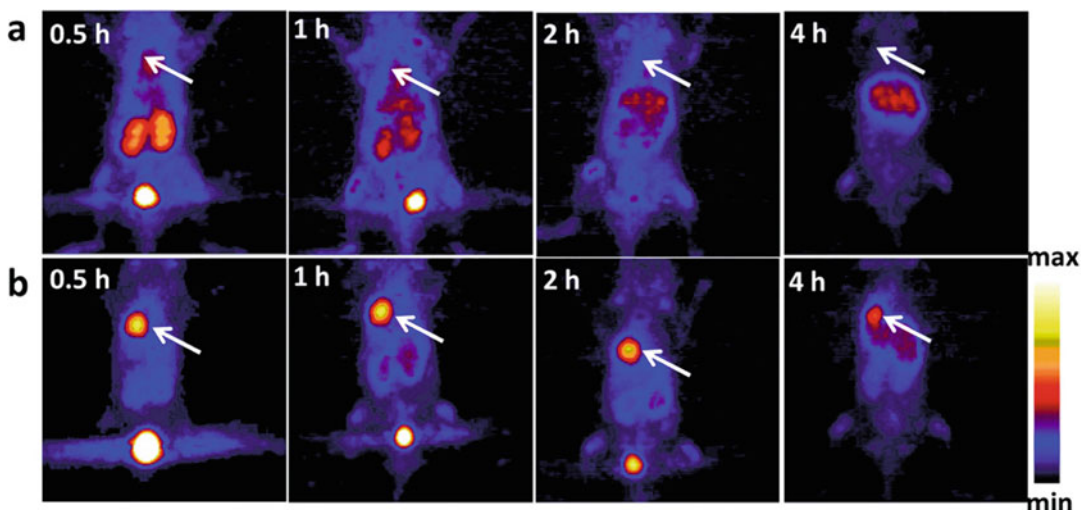


Fig. 10 In vivo PET imaging and biodistribution. Representative PET images of coronal single slices on orthotopic A549 lung tumor-bearing mice after intravenous injection of 6.7 MBq of $[^{64}\text{Cu}]\text{CuNC@BSA}$ (a) and $[^{64}\text{Cu}]\text{CuNC@BSA-LHRH}$ (b). Images were acquired at 0.5, 1, 2, and 4 h. White arrows indicate the lung tumor. Reprinted with permission from Ref. [131]

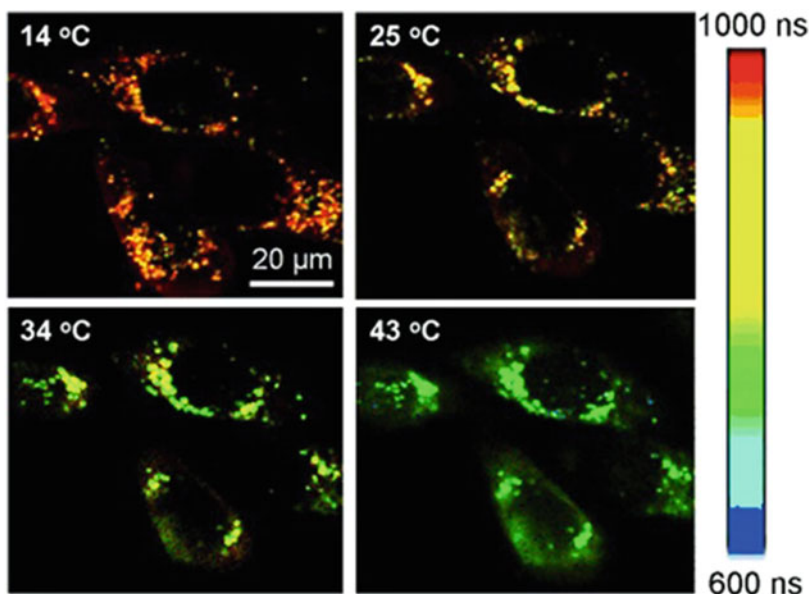


Fig. 11 Typical FLIM images of HeLa cells with internalized AuNCs at four different temperatures. Reprinted with permission from Ref. [136]

suggesting the potential of AuNC-based system for thermal sensing at the subcellular level via FLIM. In another report, Zhang and coworkers [47] demonstrated FLIM-based cellular imaging

by using MSA- and tiopronin-capped AuNCs and further covalently bound PEG moieties to improve their capability of staining HeLa cells. Particularly, they observed that these PEGylated

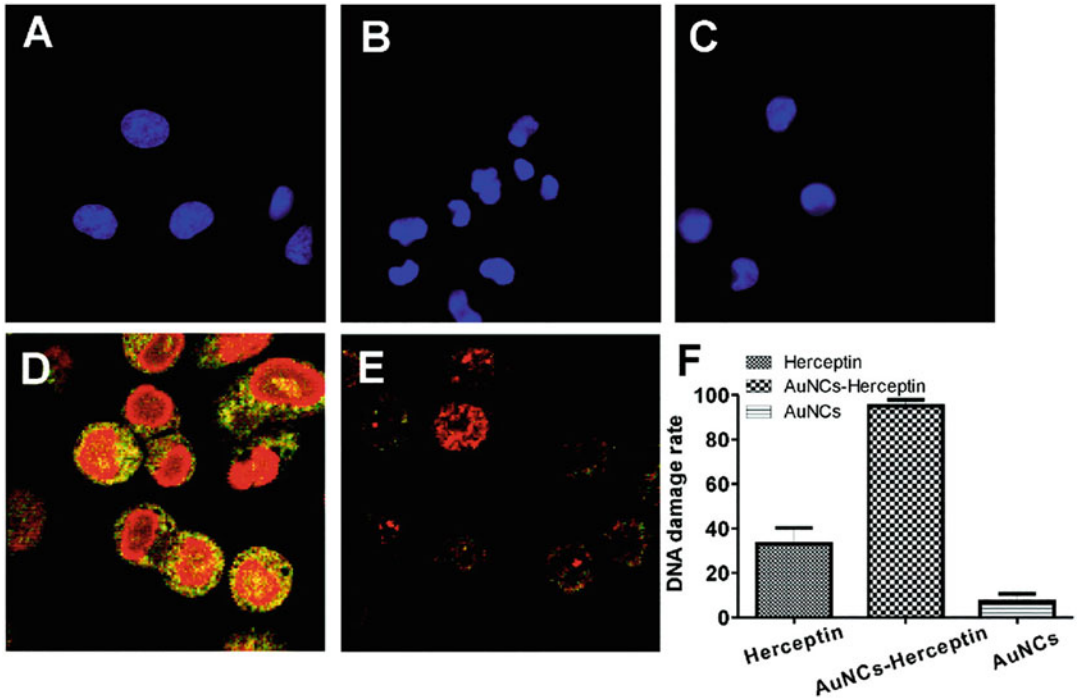


Fig. 12 Fluorescence images show the apoptosis induced by AuNCs alone (a), AuNCs-Her (b), and Herceptin (c) by staining the nucleus with Hoechst 33258 (excited by UV light and the emission is 460 nm). FLIM shows DNA damage of SK-BR3 cells induced by AuNCs-Her (d) and

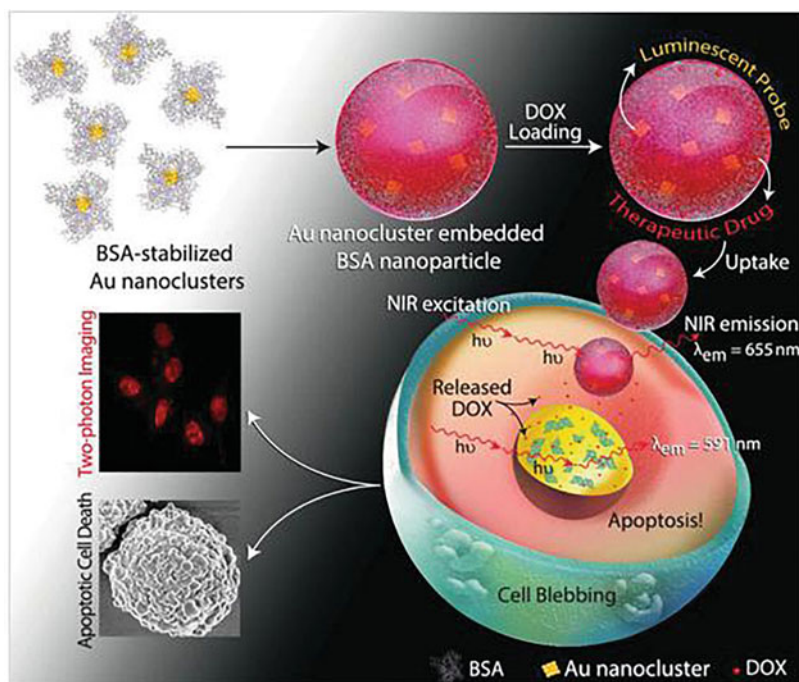
Herceptin alone (e) indicated by the bright yellow dots. Quantitative evaluation of DNA damage of cells as a percentage of the total number of cells for different treatments (f). Reprinted with permission from Ref. [137]

AuNCs widely distribute throughout the cells and especially accumulate in the areas close to the cell nucleus. Irudayaraj et al. [137] reported the use of Herceptin-conjugated BSA-AuNCs (AuNCs-Her) for simultaneous imaging and enhanced cancer therapy because of its ability to induce nuclear DNA damage and apoptosis. Importantly, they found that the endocytosed AuNCs-Her could escape the endolysosomal pathway and enter the nucleus of cancer cells to enhance the therapeutic efficacy of Herceptin. FLIM indicated that almost all of the cells cultured with AuNCs-Her had specific fluorescence staining, representing DNA damage (Fig. 12d). In contrast, only a small amount of cells treated with Herceptin alone shows DNA damage under the same condition (Fig. 12e). Quantification of apoptosis positive cells as a percentage of the total number of cells revealed that only 35% of the cells treated with Herceptin underwent apoptosis due to DNA

damage compared to 95% of the AuNCs-Her (Fig. 12f) treated cells.

The outstanding TPA cross sections of MNCs make them good candidates for application in two-photon cellular imaging, which is another attractive imaging technique because of its ability of imaging depth inside tissues and low phototoxicity of NIR light. Polavarapu and coworkers [28] investigated the two-photon excitation fluorescence imaging of SH-SY5Y human neuroblastoma cells incubated with GSH-AuNCs under excitation of femtosecond laser pulses at 800 nm. The two-photon imaging and z-stack sectioning results clearly confirmed that AuNCs were internalized inside the cells. Khandelia et al. [138] reported the use of anticancer drug doxorubicin (DOX) loaded BSA-AuNCs for imaging HeLa cells by two-photon excitation at 730 nm. Their results demonstrated that DOX-loaded AuNCs not only helped in tracking the delivery

Fig. 13 A schematic illustration of the formation of DOX-loaded AuNC-embedded BSA nanoparticles, followed by uptake and release of DOX inside HeLa cells, leading to apoptotic cell death, as visualized by two-photon imaging. Reprinted with permission from Ref. [138]



but also released drugs to the cancer cells, leading to apoptotic cell death (Fig. 13). In a recent work, Gu et al. [139] prepared RGD conjugated BSA-AuNC nano-capsules for two-photon fluorescence imaging of U87-MG cancer cells. The Z-stack sectioning of two-photon images revealed that hybrid nano-capsules were mainly resided in the cytoplasm nearby the nucleus.

4 Fluorescent MNCs as Multimodal Bioimaging Probes

At present, multimodal imaging probes based on fluorescent AuNCs for tumor imaging have also attracted plenty of attention (see the summary in Table 3). In an early work, Zhou et al. [146] reported multimodal imaging of NIR-emitting radioactive GSH-AuNPs, which were incorporated with a gold radioisotope ^{198}Au . The ^{198}Au in GSH- ^{198}Au AuNPs not only helps to quantify the pharmacokinetics of these NIR-emitting AuNPs rapidly but also allows their utility for in vivo SPECT imaging by emitting

gamma rays. Thus these NIR-emitting radioactive AuNPs can serve as dual-modality imaging probes with both SPECT and FL imaging capabilities (Fig. 14). Chen and coworkers [147] recently fabricated a dual-modality FL/CT iodinated BSA-AuNCs for early accurate diagnosis of thyroid cancer. They accomplished in vivo FL and CT imaging via an orthotopic human thyroid cancer patient tissue derived xenograft (PDX) mouse model. Adopting the similar FL and CT dual-modal imaging techniques, insulin-AuNCs were used to distinguish the differentiated C2C12 myoblasts from undifferentiated ones [148]. Also, FA-conjugated GSH-AuNCs and lysozyme-AuNCs have been used for in vivo targeted dual-modal FL/CT imaging of MGC-803 tumor-bearing mice and HeLa tumor-bearing nude mice, respectively [30, 149]. Sarkar et al. [107] synthesized protein-capped AgNCs impregnated onto GO sheets for FLIM. Furthermore, AgNCs/GO assembly have a great potential as CT imaging contrasting agents, and CT images show significant contrast enhancement of bone tissues in mice models.

Table 3 Fluorescent MNCs as multimodal bioimaging probes

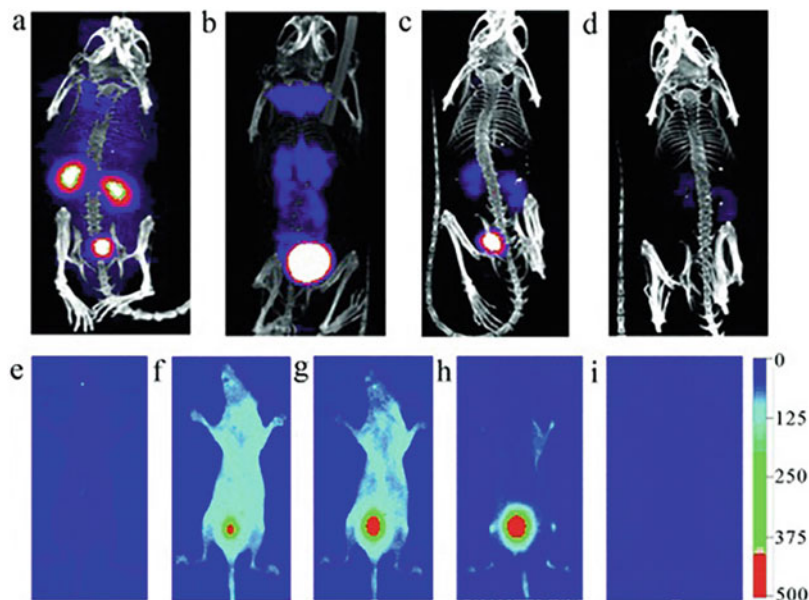
Metal	Capping agent	Functionalization	λ_{em} (nm)	Imaging modals	Biosystems	Ref.
Au	GSH	^{198}Au	810	NIRFL/SPECT	Live mouse	[146]
Au	BSA	Iodine	680	NIRFL/CT	Human thyroid cancer PDX nude mouse	[147]
Au	Insulin	–	670	NIRFL/CT	Differentiated C2C12 mouse myoblasts	[148]
Au	GSH	FA	650	NIRFL/CT	MGC-803 tumor-bearing mice	[30]
Au	Lysozyme	FA	690	NIRFL/CT	HeLa tumor-bearing nude mice	[149]
Ag	HSA, BSA	GO	620, 510	FL/CT	Swiss albino mice	[107]
Au	BSA	Gd(III)	700	NIRFL/MRI	U87-MG tumor-bearing mice	[150]
Au	Cyclodecapeptide	Gd(III)	~660	NIRFL/MRI	Kunming mouse	[151]
Au	GSH	Fe_3O_4 NPs	650	NIRFL/MRI	293 T cells	[152]
Au	BSA	Fe_3O_4 NPs	~650	NIRFL/MRI	H1650 cells	[153]
Au	BSA	Fe_3O_4 NPs, AuNRs	650	NIRFL/MRI	HeLa cells	[156]
Au	HSA	^{64}Cu	~667	NIRFL/PET	U87MG glioblastoma Xenograft mice	[134]
Au	Thioctic-zwitterion	–	~750	NIRFL/PAI	U87MG cells; mice	[164]
Au	GSH	Gd(III)	~652	NIRFL/CT/MRI	A549 tumor-bearing mice	[157]
Au	Albumin	DTPA–Gd(III)	660	NIRFL/CT/MRI	MCF-7 tumor-bearing mice	[158]
Au	BSA	Gd_2O_3 , ICG	635	NIRFL/CT/MRI	Kunming mice	[159]
Au	BSA	Gd(III), FA	660	NIRFL/CT/MRI	KB tumor-bearing mice	[161]
Au	GSH	Gd^{3+} , SiO_2	595	FL/CT/MRI	MCF-7 cells, tumor-bearing BALB/c mice	[162]
Au	Triphenylphosphine	SiO_2	827	NIRFL/PAI/MRI	LS174T tumor-bearing mice	[163]

GSH glutathione, BSA bovine serum albumin, FA folic acid, Cyclodecapeptide c (Asp-Arg-Glu-Pro-Cys-Glu-Tyr-Asp-Pro-Cys), HSA human serum albumin, GO graphene oxide, AuNRs gold nanorods, DTPA diethylene triamine pentaacetic acid, NIRFL near-infrared fluorescence, SPECT single-photon emission computed tomography, CT imaging X-ray computed tomography imaging, MRI magnetic resonance imaging, ICG indocyanine green, PET positron emission tomography, PAI photoacoustic imaging

NIRFL and MR dual-modal imaging have been reported through coupling AuNCs with magnetic agents such as Gd_2O_3 and Fe_3O_4 NPs. For example, Sun et al. [150] employed Gd_2O_3 functionalized BSA-AuNCs as probes for dual-modal NIRFL and MR blood pool imaging in vivo. By further bioconjugation of BSA- Gd_2O_3 /AuNCs with arginine–glycine–aspartic acid peptide (RGD), they can be used for in vivo targeted tumor imaging of U87-MG tumor-bearing mice. Liang and coworkers [151]

constructed Gd^{3+} -functionalized AuNCs for dual-modal NIRFL/MR imaging by using a cyclodecapeptide as the template. Recently, Wang et al. [152] demonstrated a facile strategy of fabricating GSH-AuNC probes decorated with magnetic Fe_3O_4 NPs for bimodal NIRFL/MR cell imaging. Alternatively, dual-modal bioimaging probes can be fabricated by conjugating biotinylated NIR fluorescent BSA-AuNCs to streptavidin functionalized Fe_3O_4 NPs [153].

Fig. 14 Representative SPECT images (top row) of BALB/c mice injected with GSH- ^{198}Au AuNPs. (a) 10 min, (b) 1 h, (c) 4 h, and (d) 24 h p.i. In vivo FL imaging (bottom row) of a live mouse (e) pre-injection, and (f) 5 min, (g) 20 min, (h) 1 h, (i) 24 h after IV injection of GSH- ^{198}Au AuNPs. Reprinted with permission from Ref. [146]



At present, multifunctional theranostic systems with strong clinical imaging-guided capability, phototherapy function, and target specificity have been developed for cancer therapy. Yang et al. [154] fabricated a new imaging-guided and multifunctional cancer therapy platform with multimodal imaging and dual phototherapy function by assembling the captopril-protected Au_{25}NCs ($\text{Au}_{25}(\text{Capt})_{18}^-$) into mesoporous silica-coated Nd^{3+} -sensitized upconversion nanoparticles ($\text{UCNPs}@ \text{SiO}_2$). Under 808 nm NIR irradiation, the $\text{UCNPs}@ \text{SiO}_2\text{-Au}_{25}(\text{Capt})_{18}^-$ nanocomposite can simultaneously exhibit tri-modal upconversion luminescence, photothermal, and photoacoustic imaging features in vivo. Besides, the composite can also present the MR and CT imaging effects due to the Gd^{3+} and Yb^{3+} ions in the UCNPs. Subsequently, the same group designed $\text{Fe}_3\text{O}_4@ \text{ZIF-8-Au}_{25}(\text{Capt})_{18}^-$ nanocomposites for multimodal imaging and synergistic cancer therapy [155]. Under 808 nm NIR irradiation, the attached photosensitizer agent $\text{Au}_{25}(\text{Capt})_{18}^-$ clusters can produce highly reactive singlet oxygen ($^1\text{O}_2$) for photodynamic therapy (PDT). In addition, the magnetic properties of

encapsulated Fe_3O_4 nanocrystals can simultaneously produce hyperthermal effects for photothermal therapy (PTT) and present targeting and MR imaging capability. Protein-based multifunctional nanocarriers (MFNCs) were successfully constructed by assembling gold nanorods, superparamagnetic iron oxide NPs, and AuNCs within BSA (Fig. 15) [156], without affecting their individual properties. The MFNCs showed simultaneous integration of corresponding plasmonic, magnetic, and luminescence properties, which can be used for plasmonic photothermal therapy (PPTT), two-photon and MR imaging in vitro. Moreover, the MFNCs demonstrated efficient loading and delivery of DOX to HeLa cells, resulting in efficient killing of cancer cells and tracking the delivery and release of the drug through confocal fluorescence microscopy.

In addition to the NIRFL and MRI contrasts offered by the probe, the green fluorescence of the endoperoxide triggered by $^1\text{O}_2$ can provide additional modality for live cell imaging [153]. With the co-existence of GSH-AuNCs and Gd^{3+} ions, the nanoprobe can act as a multifunctional nanoplatform for triple-modal NIRFL/CT/MR

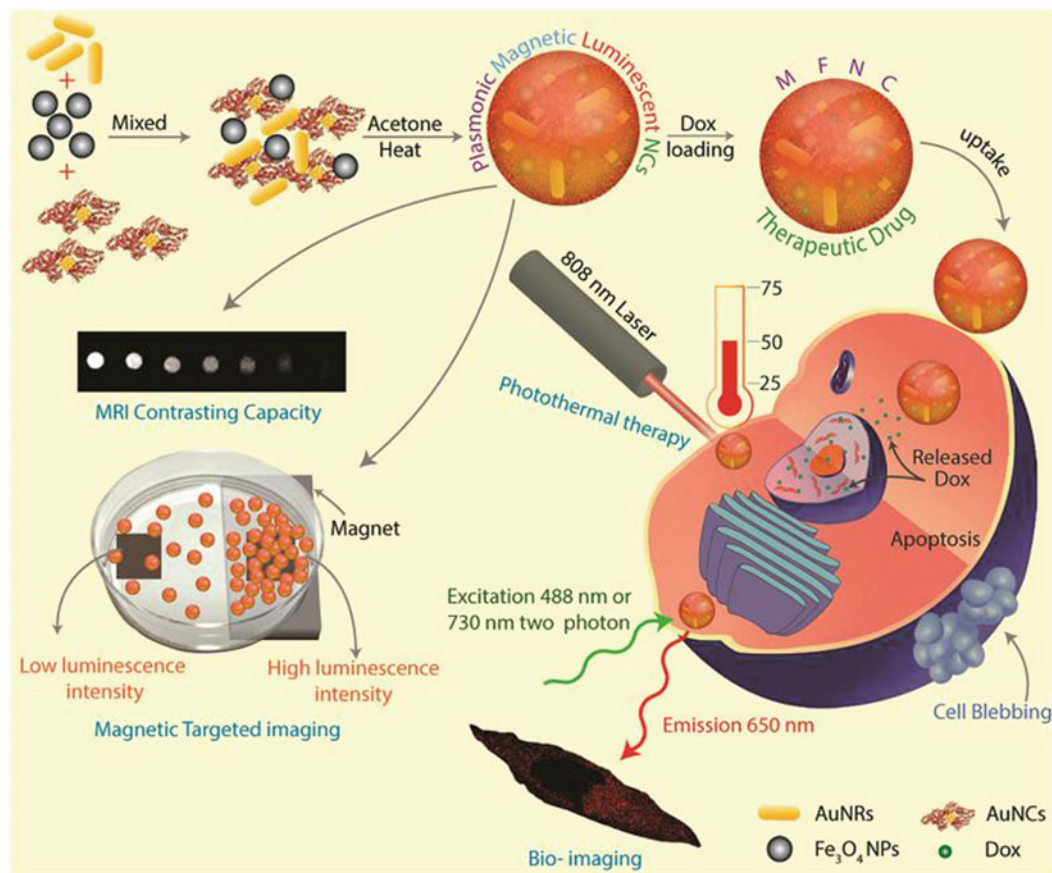


Fig. 15 Schematic depiction of preparing MFNCs, using for plasmonic photothermal therapy and two-photon/MR imaging in vitro, following successful loading and

delivery of anticancer drug Dox induced cancer cells death. Reprinted with permission from Ref. [156]

imaging of A549 cancer cells and xenografted A549 tumor models [157]. Similarly, Hu and coworkers [158] prepared Au–Gd NC hybrids by using albumin as the stabilizer, which were suitable for in vivo triple-modal NIRFL/CT/MRI imaging of MCF-7 tumor-bearing mice (Fig. 16). Upon intravenously injected, the hybrid NCs were effectively accumulated in tumor tissues and quickly cleared by renal excretion, indicating their capacity of tumor targeting and low body residues. Recently, Wang and coworkers [159] developed a facile approach to construct BSA-stabilized Gd₂O₃-AuNCs nanoplatform for multimodal imaging and cancer therapy. The nanocomposites exhibit photoluminescent

capability in NIR region, and are able to generate singlet oxygen (¹O₂) species under NIR laser irradiation at 808 nm for photodynamic therapy. After loading indocyanine green (ICG), the Gd₂O₃-AuNCs-ICG nanocomposites exhibited excellent in vivo triple-modal NIRFL/MR/CT imaging capability, as well as combined photodynamic and photothermal therapy. Wang et al. [160] reported a new method for targeted multi-modal tumor bioimaging by using in situ self-synthesized AuNCs and iron complexes composites via simple introduction of AuCl₄⁻ (i.e., HAuCl₄) and Fe²⁺ (i.e., FeCl₂) ions to the cancer cells or xenograft tumor mice model. In a recent study, the same group [39] explored a

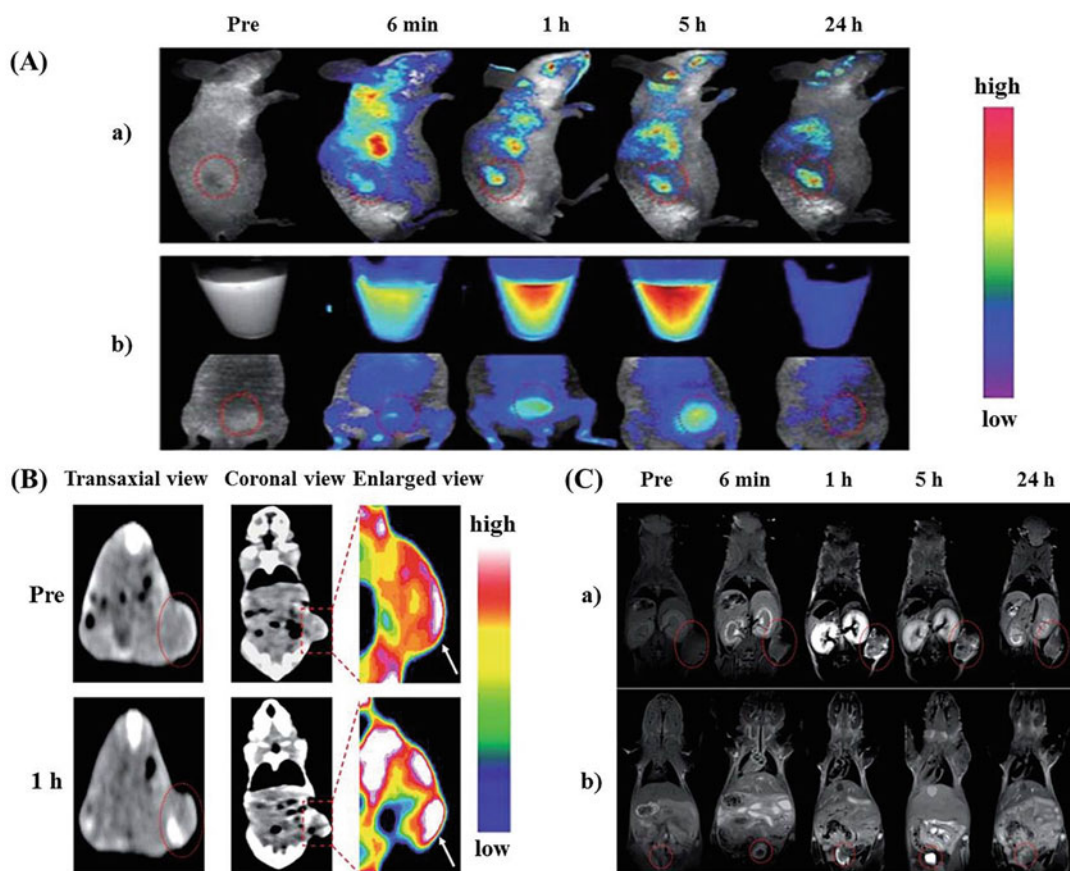


Fig. 16 (a) (a and b) In vivo FL imaging of MCF-7 tumor-bearing mice after the tail-vein injection of hybrid NCs. Inset image is the FL reflectance images of urine. (b) In vivo CT images of MCF-7 tumor-bearing mice injected with the hybrid Au-Gd NCs. The arrow and red dotted

circle indicate the tumor site. (c) (a and b) In vivo MRI images of MCF-7 tumor-bearing mice injected with the hybrid Au-Gd NCs. The arrow and red dotted circle indicate the tumor (a) and bladder (b) sites, respectively. Reprinted with permission from Ref. [158]

novel in vivo multimodal NIRFL/MR/CT bioimaging method for the early detection of tumors based on in situ biosynthesized Zn&Fe oxide NCs. By introducing Zn^{2+} and Fe^{2+} ions via a single injection, fluorescent ZnO NCs and superparamagnetic Fe_3O_4 nanoparticles can be spontaneously self-biosynthesized in tumor cells/tissues. Xu et al. [161] synthesized AuNC-Gd₂O₃ integrated nanoprobe (denoted as AuGds) using BSA as the template via a biomineralization approach. After being chemically modified with FA, the FA-AuGds could specifically target FRs on KB tumor cells, and permitted in vivo NIRFL, MR, and CT imaging of xenografted KB tumor-

bearing mice. Gd³⁺-aggregated AuNCs encapsulated by SiO₂ shell (Gd³⁺-AuNCs@SiO₂ NPs) were strategically designed and prepared. In the presence of Gd³⁺ ions, the GSH-capped AuNCs show aggregation-induced fluorescence (AEF) effect. The as-prepared composites can be used for in vitro and in vivo multimodal FL/MR/CT cancer imaging [162]. Hembury and coworkers [163] synthesized highly monodispersed SiO₂/AuNCs by nucleating gold within hollow mesoporous silica particles in a one-phase synthetic route. These SiO₂/AuNCs possessed stable NIR fluorescence and paramagnetism, thus it could be used as a promising probe

for in vivo NIRFL/PAI/MR imaging of colorectal carcinoma tumor (LS174T)-bearing mice.

5 Conclusions and Outlooks

In this chapter, we have systematically summarized recent advances in the synthesis strategies and bioimaging applications of fluorescent MNCs. In the past few years, fluorescent MNCs have been largely explored for bioimaging due to their ultrasmall size, good biocompatibility, and easy functionalization. Although a large number of researches have been reported about MNCs currently, there are still a lot of rooms to further improve and many unclear questions to reveal.

First of all, most MNCs possess a relatively low QY (usually less than 10%) in comparison to other fluorophores such as semiconductor QDs and many organic dyes. In addition, MNCs often show size heterogeneity in the crude product, and it still remains challenging to obtain atomically precise water-soluble MNCs suitable for bioimaging applications, which markedly precludes quantitative tracking in organisms. Therefore, researchers still need to make greater effort to explore more efficient synthesis routes for size-controllable fluorescent MNCs with relatively high QY and high purity [165, 166]. Second, the present bioimaging studies mainly concentrate on fluorescent AuNCs due to their good stability and easy synthesis. Considering gold is relatively expensive compared to other metals, it would be attractive to further exploit potential bioimaging applications of other MNCs or alloy NCs. Third, up to now, relatively little is known about the behavior of these ultrasmall MNCs within the complex biological environment [167], which is actually highly important regarding the safe as well as efficient use of MNCs in bioimaging applications. Thus, further study to understand the mechanism of cellular and intravital uptake of MNCs and long-term effect after entering into biosystems would be necessary and important. Furthermore, in order to advance potential utility of MNCs as multifunctional probes for applications besides

imaging, more types of MNCs-based nanocomposites should be developed by integrating other functional nanomaterials.

In the past years, significant progress has been achieved in developing fluorescent MNCs for bioimaging, but many challenges still remain to face and resolve in the future. With continuing development and more efforts within the community, we believe that more robust fluorescent MNCs will be available, which will then further advance imaging-based applications of these novel nanoprobes in medical diagnose and therapy researches.

Acknowledgements This chapter was modified from the paper published by our group in Chinese Chemical Letters (Xu and Shang 2018; 29:1436–1444). The related contents are re-used with the permission.

References

1. Díez I, Ras RHA (2010) Few-atom silver clusters as fluorescent reporters. In: *Advanced fluorescence reporters in chemistry and biology II*. Springer, Dordrecht, pp 307–332
2. Zheng J, Nicovich PR, Dickson RM (2007) Highly fluorescent noble-metal quantum dots. *Annu Rev Phys Chem* 58:409–431
3. Díez I, Ras RHA (2011) Fluorescent silver nanoclusters. *Nanoscale* 3:1963–1970
4. He X, Wang K, Cheng Z (2010) In vivo near-infrared fluorescence imaging of cancer with nanoparticle-based probes. *WIREs Nanomed Nanobiotechnol* 2:349–366
5. Song F, Liang R, Deng J, Liu Z, Peng X (2017) Fine-tailoring the linker of near-infrared fluorescence probes for nitroreductase imaging in hypoxic tumor cells. *Chin Chem Lett* 28:1997–2000
6. Park H, Crozier KB (2013) Multispectral imaging with vertical silicon nanowires. *Sci Rep* 3:2460
7. He X, Gao J, Gambhir SS, Cheng Z (2010) Near-infrared fluorescent nanoprobes for cancer molecular imaging: status and challenges. *Trends Mol Med* 16:574–583
8. Weng J, Ren J (2006) Luminescent quantum dots: a very attractive and promising tool in biomedicine. *Curr Med Chem* 13:897–909
9. Berezin MY, Achilefu S (2010) Fluorescence lifetime measurements and biological imaging. *Chem Rev* 110:2641–2684
10. Helmchen F, Denk W (2005) Deep tissue two-photon microscopy. *Nat Methods* 2:932–940
11. Shang L, Azadfar N, Stockmar F, Send W, Trouillet V, Bruns M, Gerthsen D, Nienhaus GU

- (2011) One-pot synthesis of near-infrared fluorescent gold clusters for cellular fluorescence lifetime imaging. *Small* 7:2614–2620
12. Yuan L, Lin W, Zheng K, He L, Huang W (2013) Far-red to near infrared analyte-responsive fluorescent probes based on organic fluorophore platforms for fluorescence imaging. *Chem Soc Rev* 42:622–661
 13. Kim HM, Jung C, Kim BR, Jung SY, Hong JH, Ko YG, Lee KJ, Cho BR (2007) Environment-sensitive two-photon probe for intracellular free magnesium ions in live tissue. *Angew Chem Int Ed* 46:3460–3463
 14. Zipfel WR, Williams RM, Webb WW (2003) Non-linear magic: multiphoton microscopy in the biosciences. *Nat Biotechnol* 21:1369–1377
 15. Lee DE, Koo H, Sun IC, Ryu JH, Kim K, Kwon IC (2012) Multifunctional nanoparticles for multimodal imaging and theragnosis. *Chem Soc Rev* 41:2656–2672
 16. Li DZ, Chen HD, Bi F, Wang ZX (2016) Progress of multimodal molecular imaging technology in diagnosis of tumor. *Chin J Anal Chem* 44:1609–1618
 17. Willmann JK, van Bruggen N, Dinkelborg LM, Gambhir SS (2008) Molecular imaging in drug development. *Nature Rev Drug Discov* 7:591–607
 18. Zhou B, Zheng L, Peng C, Li D, Li J, Wen S, Shen M, Zhang G, Shi X (2014) Synthesis and characterization of PEGylated polyethylenimine-entrapped gold nanoparticles for blood pool and tumor CT imaging. *ACS Appl Mater Interfaces* 6:17190–17199
 19. Peng C, Qin J, Zhou B, Chen Q, Shen M, Zhu M, Lu X, Shi X (2013) Targeted tumor CT imaging using folic acid-modified PEGylated dendrimer-entrapped gold nanoparticles. *Polym Chem* 4:4412–4424
 20. Zhou J, Lu Z, Shan G, Wang S, Liao Y (2014) Gadolinium complex and phosphorescent probe-modified NaDyF₄ nanorods for T1- and T2-weighted MRI/CT/phosphorescence multimodality imaging. *Biomaterials* 35:368–377
 21. Kim J, Piao Y, Hyeon T (2009) Multifunctional nanostructured materials for multimodal imaging, and simultaneous imaging and therapy. *Chem Soc Rev* 38:372–390
 22. Tsotsalas M, Busby M, Gianolio E, Aime S, De Cola L (2008) Functionalized nanocontainers as dual magnetic and optical probes for molecular imaging applications. *Chem Mater* 20:5888–5893
 23. Lee JH, Huh YM, Jun YW, Seo JW, Jang JT, Song HT, Kim S, Cho EJ, Yoon HG, Suh JS, Cheon J (2007) Artificially engineered magnetic nanoparticles for ultra-sensitive molecular imaging. *Nat Med* 13:95–99
 24. Michaelis J, Hettich C, Mlynek J, Sandoghdar V (2000) Optical microscopy using a single-molecule light source. *Nature* 405:325–328
 25. Louie A (2010) Multimodality imaging probes: design and challenges. *Chem Rev* 110:3146–3195
 26. Lu Y, Chen W (2012) Sub-nanometre sized metal clusters: from synthetic challenges to the unique property discoveries. *Chem Soc Rev* 41:3594–3623
 27. Jin R (2010) Quantum sized, thiolate-protected gold nanoclusters. *Nanoscale* 2:343–362
 28. Polavarapu L, Manna M, Xu QH (2011) Biocompatible glutathione capped gold clusters as one- and two-photon excitation fluorescence contrast agents for live cells imaging. *Nanoscale* 3:429–434
 29. Liu J, Yu M, Zhou C, Yang S, Ning X, Zheng J (2013) Passive tumor targeting of renal-clearable luminescent gold nanoparticles: long tumor retention and fast normal tissue clearance. *J Am Chem Soc* 135:4978–4981
 30. Zhang C, Zhou Z, Qian Q, Gao G, Li C, Feng L, Wang Q, Cui D (2013) Glutathione-capped fluorescent gold nanoclusters for dual-modal fluorescence/X-ray computed tomography imaging. *J Mater Chem B* 1:5045–5053
 31. Yang J, Xia N, Wang X, Liu X, Xu A, Wu Z, Luo Z (2015) One-pot one-cluster synthesis of fluorescent and bio-compatible Ag₁₄ nanoclusters for cancer cell imaging. *Nanoscale* 7:18464–18470
 32. Pyo K, Thanthirige VD, Kwak K, Pandurangan P, Ramakrishna G, Lee D (2015) Ultrabright luminescence from gold nanoclusters: rigidifying the Au(I)-thiolate shell. *J Am Chem Soc* 137:8244–8250
 33. Li Y, Wang X, Xu S, Xu W (2013) The solvent effect on the luminescence of silver nanoclusters. *Phys Chem Chem Phys* 15:2665–2668
 34. Wang C, Wu J, Jiang K, Humphrey MG, Zhang C (2017) Stable Ag nanoclusters-based nano-sensors: rapid sonochemical synthesis and detecting Pb²⁺ in living cells. *Sens Actuators B Chem* 238:1136–1143
 35. Wang C, Ling L, Yao Y, Song Q (2015) One-step synthesis of fluorescent smart thermo-responsive copper clusters: a potential nanothermometer in living cells. *Nano Res* 8:1975–1986
 36. Wang J, Zhang G, Li Q, Jiang H, Liu C, Amatore C, Wang X (2013) In vivo self-bio-imaging of tumors through in situ biosynthesized fluorescent gold nanoclusters. *Sci Rep* 3:1157
 37. Gao S, Chen D, Li Q, Ye J, Jiang H, Amatore C, Wang X (2014) Near-infrared fluorescence imaging of cancer cells and tumors through specific biosynthesis of silver nanoclusters. *Sci Rep* 4:4384
 38. Ye J, Dong X, Jiang H, Wang X (2017) An intracellular temperature nanoprobe based on biosynthesized fluorescent copper nanoclusters. *J Mater Chem B* 5:691–696
 39. Du T, Zhao C, ur Rehman F, Lai L, Li X, Sun Y, Luo S, Jiang H, Selke M, Wang X (2017) Rapid and multimodal in vivo bioimaging of cancer cells through in situ biosynthesis of Zn&Fe nanoclusters. *Nano Res* 10:2626–2632
 40. Wang C, Wang Y, Xu L, Zhang D, Liu M, Li X, Sun H, Lin Q, Yang B (2012) Facile aqueous-phase synthesis of biocompatible and fluorescent Ag₂S nanoclusters for bioimaging: tunable

- photoluminescence from red to near infrared. *Small* 8:3137–3142
41. Ding C, Cao X, Zhang C, He T, Hua N, Xian Y (2017) Rare earth ions enhanced near infrared fluorescence of Ag₂S quantum dots for the detection of fluoride ions in living cells. *Nanoscale* 9:14031–14038
 42. Wang C, Xu L, Xu X, Cheng H, Sun H, Lin Q, Zhang C (2014) Near infrared Ag/Au alloy nanoclusters: tunable photoluminescence and cellular imaging. *J Colloid Interface Sci* 416:274–279
 43. Sun Y, Xia Y (2004) Mechanistic study on the replacement reaction between silver nanostructures and chloroauric acid in aqueous medium. *J Am Chem Soc* 126:3892–3901
 44. Shang L, Yang L, Stockmar F, Popescu R, Trouillet V, Bruns M, Gerthsen D, Nienhaus GU (2012) Microwave-assisted rapid synthesis of luminescent gold nanoclusters for sensing Hg²⁺ in living cells using fluorescence imaging. *Nanoscale* 4:4155–4160
 45. Nair LV, Nazeer SS, Jayasree RS, Ajayaghosh A (2015) Fluorescence imaging assisted photodynamic therapy using photosensitizer-linked gold quantum clusters. *ACS Nano* 9:5825–5832
 46. Ghosh R, Goswami U, Ghosh SS, Paul A, Chattopadhyay A (2015) Synergistic anticancer activity of fluorescent copper nanoclusters and cisplatin delivered through a hydrogel nanocarrier. *ACS Appl Mater Interfaces* 7:209–222
 47. Zhang J, Fu Y, Conroy CV, Tang Z, Li G, Zhao RY, Wang G (2012) Fluorescence intensity and lifetime cell imaging with luminescent gold nanoclusters. *J Phys Chem C* 116:26561–26569
 48. Pan S, Liu W, Tang J, Yang Y, Feng H, Qian Z, Zhou J (2018) Hydrophobicity-guided self-assembled particles of silver nanoclusters with aggregation-induced emission and their use in sensing and bioimaging. *J Mater Chem B* 6:3927–3933
 49. Muhammed MAH, Verma PK, Pal SK, Kumar RCA, Paul S, Omkumar RV, Pradeep T (2009) Bright, NIR-emitting Au₂₃ from Au₂₅: characterization and applications including biolabeling. *Chem Eur J* 15:10110–10120
 50. Le Guével X, Spies C, Daum N, Jung G, Schneider M (2012) Highly fluorescent silver nanoclusters stabilized by glutathione: a promising fluorescent label for bioimaging. *Nano Res* 5:379–387
 51. Lin CAJ, Yang TY, Lee CH, Huang SH, Sperling RA, Zanella M, Li JK, Shen JL, Wang HH, Yeh HI (2009) Synthesis, characterization, and bioconjugation of fluorescent gold nanoclusters toward biological labeling applications. *ACS Nano* 3:395–401
 52. Wang HH, Lin CAJ, Lee CH, Lin YC, Tseng YM, Hsieh CL, Chen CH, Tsai CH, Hsieh CT, Shen JL, Chan WH, Chang WH, Yeh HI (2011) Fluorescent gold nanoclusters as a biocompatible marker for in vitro and in vivo tracking of endothelial cells. *ACS Nano* 5:4337–4344
 53. Shang L, Dong S, Nienhaus GU (2011) Ultra-small fluorescent metal nanoclusters: synthesis and biological applications. *Nano Today* 6:401–418
 54. Shang L, Nienhaus GU (2015) Biomaterialization: nanocrystals by design. *Nat Chem* 7:769–770
 55. Xie J, Zheng Y, Ying JY (2009) Protein-directed synthesis of highly fluorescent gold nanoclusters. *J Am Chem Soc* 131:888–889
 56. Yu X, Liu W, Deng X, Yan S, Su Z (2018) Gold nanocluster embedded bovine serum albumin nanofibers-graphene hybrid membranes for the efficient detection and separation of mercury ion. *Chem Eng J* 335:176–184
 57. Wang Y, Chen JT, Yan XP (2013) Fabrication of transferrin functionalized gold nanoclusters/graphene oxide nanocomposite for turn-on near-infrared fluorescent bioimaging of cancer cells and small animals. *Anal Chem* 85:2529–2535
 58. Sun C, Yang H, Yuan Y, Tian X, Wang L, Guo Y, Xu L, Lei J, Gao N, Anderson GJ, Liang XJ, Chen C, Zhao Y, Nie G (2011) Controlling assembly of paired gold clusters within apoferritin nanoreactor for in vivo kidney targeting and biomedical imaging. *J Am Chem Soc* 133:8617–8624
 59. Le Guevel X, Daum N, Schneider M (2011) Synthesis and characterization of human transferrin-stabilized gold nanoclusters. *Nanotechnology* 22:275103
 60. Liu JM, Chen JT, Yan XP (2013) Near infrared fluorescent trypsin stabilized gold nanoclusters as surface plasmon enhanced energy transfer biosensor and in vivo cancer imaging bioprobe. *Anal Chem* 85:3238–3245
 61. Liu CL, Liu TM, Hsieh TY, Liu HW, Chen YS, Tsai CK, Chen HC, Lin JW, Hsu RB, Wang TD, Chen CC, Sun CK, Chou PT (2013) In vivo metabolic imaging of insulin with multiphoton fluorescence of human insulin-Au nanodots. *Small* 9:2103–2110
 62. Kong Y, Chen J, Gao F, Brydson R, Johnson B, Heath G, Zhang Y, Wu L, Zhou D (2013) Near-infrared fluorescent ribonuclease-A-encapsulated gold nanoclusters: preparation, characterization, cancer targeting and imaging. *Nanoscale* 5:1009–1017
 63. Zhao T, He XW, Li WY, Zhang YK (2015) Transferrin-directed preparation of red-emitting copper nanoclusters for targeted imaging of transferrin receptor over-expressed cancer cells. *J Mater Chem B* 3:2388–2394
 64. Liu F, Bing T, Shangguan D, Zhao M, Shao N (2016) Ratiometric fluorescent biosensing of hydrogen peroxide and hydroxyl radical in living cells with lysozyme-silver nanoclusters: lysozyme as stabilizing ligand and fluorescence signal unit. *Anal Chem* 88:10631–10638
 65. Muhammed MAH, Verma PK, Pal SK, Retnakumari A, Koyakutty M, Nair S, Pradeep T (2010) Luminescent quantum clusters of gold in

- bulk by albumin-induced core etching of nanoparticles: metal ion sensing, metal-enhanced luminescence, and biolabeling. *Chem Eur J* 16:10103–10112
66. Yuan Q, Wang Y, Zhao L, Liu R, Gao F, Gao L, Gao X (2016) Peptide protected gold clusters: chemical synthesis and biomedical applications. *Nanoscale* 8:12095–12104
67. Yu X, Wang Z, Su Z, Wei G (2017) Design, fabrication, and biomedical applications of bioinspired peptide–inorganic nanomaterial hybrids. *J Mater Chem B* 5:1130–1142
68. Wang Y, Cui Y, Zhao Y, Liu R, Sun Z, Li W, Gao X (2012) Bifunctional peptides that precisely biomaterialize Au clusters and specifically stain cell nuclei. *Chem Commun* 48:871–873
69. Zhang W, Lin D, Wang H, Li J, Nienhaus GU, Su Z, Wei G, Shang L (2017) Supramolecular self-assembly bioinspired synthesis of luminescent gold nanocluster-embedded peptide nanofibers for temperature sensing and cellular imaging. *Bioconjug Chem* 28:2224–2229
70. Pichiaya S, Krishnan Y (2006) First blueprint, now bricks: DNA as construction material on the nanoscale. *Chem Soc Rev* 35:1111–1121
71. Richards CI, Choi S, Hsiang JC, Antoku Y, Vosch T, Bongiorno A, Tzeng YL, Dickson RM (2008) Oligonucleotide-stabilized Ag nanocluster fluorophores. *J Am Chem Soc* 130:5038–5039
72. Sharma J, Yeh HC, Yoo H, Werner JH, Martinez JS (2010) A complementary palette of fluorescent silver nanoclusters. *Chem Commun* 46:3280–3282
73. Shukla S, Sastry M (2009) Probing differential Ag +–nucleobase interactions with isothermal titration calorimetry (ITC): towards patterned DNA metallization. *Nanoscale* 1:122–127
74. Soto-Verdugo V, Metiu H, Gwinn E (2010) The properties of small Ag clusters bound to DNA bases. *J Chem Phys* 132:195102
75. Schultz D, Gwinn E (2011) Stabilization of fluorescent silver clusters by RNA homopolymers and their DNA analogs: C,G versus A,T(U) dichotomy. *Chem Commun* 47:4715–4717
76. Vosch T, Antoku Y, Hsiang JC, Richards CI, Gonzalez JI, Dickson RM (2007) Strongly emissive individual DNA-encapsulated Ag nanoclusters as single-molecule fluorophores. *Proc Natl Acad Sci U S A* 104:12616–12621
77. Antoku Y, Hotta J, Mizuno H, Dickson RM, Hofkens J, Vosch T (2010) Transfection of living HeLa cells with fluorescent poly-cytosine encapsulated Ag nanoclusters. *Photochem Photobiol Sci* 9:716–721
78. Ai J, Guo W, Li B, Li T, Li D, Wang E (2012) DNA G-quadruplex-templated formation of the fluorescent silver nanocluster and its application to bioimaging. *Talanta* 88:450–455
79. Yin J, He X, Wang K, Qing Z, Wu X, Shi H, Yang X (2012) One-step engineering of silver nanoclusters-aptamer assemblies as luminescent labels to target tumor cells. *Nanoscale* 4:110–112
80. Yin J, He X, Wang K, Xu F, Shangguan J, He D, Shi H (2013) Label-free and turn-on aptamer strategy for cancer cells detection based on a DNA-silver nanocluster fluorescence upon recognition-induced hybridization. *Anal Chem* 85:12011–12019
81. Huang X, Luo Y, Li Z, Li B, Zhang H, Li L, Majeed I, Zou P, Tan B (2011) Biolabeling hematopoietic system cells using near-infrared fluorescent gold nanoclusters. *J Phys Chem C* 115:16753–16763
82. Liu J, Yu M, Ning X, Zhou C, Yang S, Zheng J (2013) PEGylation and zwitterionization: pros and cons in the renal clearance and tumor targeting of near-IR-emitting gold nanoparticles. *Angew Chem Int Ed* 52:12572–12576
83. Wang Y, Dai C, Yan XP (2014) Fabrication of folate bioconjugated near-infrared fluorescent silver nanoclusters for targeted in vitro and in vivo bioimaging. *Chem Commun* 50:14341–14344
84. Tanaka S, Miyazaki J, Tiwari DK, Jin T, Inouye Y (2011) Fluorescent platinum nanoclusters: synthesis, purification, characterization, and application to bioimaging. *Angew Chem Int Ed* 50:431–435
85. Huang X, Ishitobi H, Inouye Y (2016) Formation of fluorescent platinum nanoclusters using hyperbranched polyethylenimine and their conjugation to antibodies for bio-imaging. *RSC Adv* 6:9709–9716
86. Yang L, Wang H, Li D, Li L, Lou X, Liu H (2018) Self-nucleation and self-assembly of highly fluorescent Au₅ nanoclusters for bioimaging. *Chem Mater* 30:5507–5515
87. Yam VWW, Cheng ECC, Zhou ZY (2000) A highly soluble luminescent decanuclear gold(I) complex with a propeller-shaped structure. *Angew Chem Int Ed* 39:1683–1685
88. Das NK, Ghosh S, Priya A, Datta S, Mukherjee S (2015) Luminescent copper nanoclusters as a specific cell-imaging probe and a selective metal ion sensor. *J Phys Chem C* 119:24657–24664
89. Kong L, Chu X, Liu W, Yao Y, Zhu P, Ling X (2016) Glutathione-directed synthesis of Cr(vi)- and temperature-responsive fluorescent copper nanoclusters and their applications in cellular imaging. *New J Chem* 40:4744–4750
90. Ge W, Zhang Y, Ye J, Chen D, Rehman FU, Li Q, Chen Y, Jiang H, Wang X (2015) Facile synthesis of fluorescent Au/Ce nanoclusters for high-sensitive bioimaging. *J Nanobiotechnol* 13:8
91. Huang H, Li H, Feng JJ, Wang AJ (2016) One-step green synthesis of fluorescent bimetallic Au/Ag nanoclusters for temperature sensing and in vitro detection of Fe³⁺. *Sens Actuators B Chem* 223:550–556
92. Wang P, Lin L, Guo Z, Chen J, Tian H, Chen X, Yang H (2016) Highly fluorescent gene carrier based on Ag-Au alloy nanoclusters. *Macromol Biosci* 16:160–167

93. Desai ML, Jha S, Basu H, Singhal RK, Sharma PK, Kailasa SK (2018) Chicken egg white and L-cysteine as cooperative ligands for effective encapsulation of Zn-doped silver nanoclusters for sensing and imaging applications. *Colloid Surface A* 559:35–42
94. Shang L, Dörlich RM, Trouillet V, Bruns M, Nienhaus GU (2012) Ultrasmall fluorescent silver nanoclusters: protein adsorption and its effects on cellular responses. *Nano Res* 5:531–542
95. Cao H, Chen Z, Zheng H, Huang Y (2014) Copper nanoclusters as a highly sensitive and selective fluorescence sensor for ferric ions in serum and living cells by imaging. *Biosens Bioelectron* 62:189–195
96. Liu CL, Ho ML, Chen YC, Hsieh CC, Lin YC, Wang YH, Yang MJ, Duan HS, Chen BS, Lee JF, Hsiao JK, Chou PT (2009) Thiol-functionalized gold nanodots: two-photon absorption property and imaging in vitro. *J Phys Chem C* 113:21082–21089
97. Bian P, Zhou J, Liu Y, Ma Z (2013) One-step fabrication of intense red fluorescent gold nanoclusters and their application in cancer cell imaging. *Nanoscale* 5:6161–6166
98. Shang L, Dorlich RM, Brandholt S, Schneider R, Trouillet V, Bruns M, Gerthsen D, Nienhaus GU (2011) Facile preparation of water-soluble fluorescent gold nanoclusters for cellular imaging applications. *Nanoscale* 3:2009–2014
99. Hu S, Ye B, Yi X, Cao Z, Wu D, Shen C, Wang J (2016) Dumbbell-shaped metallothionein-templated silver nanoclusters with applications in cell imaging and Hg²⁺ sensing. *Talanta* 155:272–277
100. Chandirasekar S, Chandrasekaran C, Muthukumarasamyvel T, Sudhandiran G, Rajendiran N (2015) Sodium cholate-templated blue light-emitting Ag subnanoclusters: in vivo toxicity and imaging in zebrafish embryos. *ACS Appl Mater Interfaces* 7:1422–1430
101. Wu X, He X, Wang K, Xie C, Zhou B, Qing Z (2010) Ultrasmall near-infrared gold nanoclusters for tumor fluorescence imaging in vivo. *Nanoscale* 2:2244–2249
102. Chen H, Li S, Li B, Ren X, Li S, Mahounga DM, Cui S, Gu Y, Achilefu S (2012) Folate-modified gold nanoclusters as near-infrared fluorescent probes for tumor imaging and therapy. *Nanoscale* 4:6050–6064
103. Le Guével X, Hötzer B, Jung G, Schneider M (2011) NIR-emitting fluorescent gold nanoclusters doped in silica nanoparticles. *J Mater Chem* 21:2974–2981
104. Retnakumari A, Setua S, Menon D, Ravindran P, Muhammed H, Pradeep T, Nair S, Koyakutty M (2010) Molecular-receptor-specific, non-toxic, near-infrared-emitting Au cluster-protein nanoconjugates for targeted cancer imaging. *Nanotechnology* 21:055103
105. Sarparast M, Noori A, Ilkhani H, Bathaie SZ, El-Kady MF, Wang LJ, Pham H, Marsh KL, Kaner RB, Mousavi MF (2016) Cadmium nanoclusters in a protein matrix: synthesis, characterization, and application in targeted drug delivery and cellular imaging. *Nano Res* 9:3229–3246
106. Pandya A, Tripathi A, Purohit R, Singh S, Nandasiri MI, Karakoti A, Singh SP, Shanker R (2015) Fluorescent magnesium nanocomplex in a protein scaffold for cell nuclei imaging applications. *RSC Adv* 5:94236–94240
107. Kundu N, Mukherjee D, Maiti TK, Sarkar N (2017) Protein-guided formation of silver nanoclusters and their assembly with graphene oxide as an improved bioimaging agent with reduced toxicity. *J Phys Chem Lett* 8:2291–2297
108. Wang Y, Cui Y, Liu R, Wei Y, Jiang X, Zhu H, Gao L, Zhao Y, Chai Z, Gao X (2013) Blue two-photon fluorescence metal cluster probe precisely marking cell nuclei of two cell lines. *Chem Commun* 49:10724–10726
109. Ghosh R, Sahoo AK, Ghosh SS, Paul A, Chattopadhyay A (2014) Blue-emitting copper nanoclusters synthesized in the presence of lysozyme as candidates for cell labeling. *ACS Appl Mater Interfaces* 6:3822–3828
110. Tian L, Li Y, Ren T, Tong Y, Yang B, Li Y (2017) Novel bimetallic gold-silver nanoclusters with “Synergy”-enhanced fluorescence for cyanide sensing, cell imaging and temperature sensing. *Talanta* 170:530–539
111. Wang X, Wang Y, He H, Ma X, Chen Q, Zhang S, Ge B, Wang S, Nau WM, Huang F (2017) Deep-red fluorescent gold nanoclusters for nucleoli staining: real-time monitoring of the nucleolar dynamics in reverse transformation of malignant cells. *ACS Appl Mater Interfaces* 9:17799–17806
112. Li J, Zhong X, Cheng F, Zhang JR, Jiang LP, Zhu JJ (2012) One-pot synthesis of aptamer-functionalized silver nanoclusters for cell-type-specific imaging. *Anal Chem* 84:4140–4146
113. Zhu X, Shi H, Shen Y, Zhang B, Zhao J, Li G (2015) A green method of staining DNA in polyacrylamide gel electrophoresis based on fluorescent copper nanoclusters synthesized in situ. *Nano Res* 8:2714–2720
114. Tian H, Guo Z, Chen J, Lin L, Xia J, Dong X, Chen X (2012) PEI conjugated gold nanoparticles: efficient gene carriers with visible fluorescence. *Adv Healthc Mater* 1:337–341
115. Li Y, Feng L, Yan W, Hussain I, Su L, Tan B (2019) PVP-templated highly luminescent copper nanoclusters for sensing trinitrophenol and living cell imaging. *Nanoscale* 11:1286–1294
116. Shang L, Yang L, Seiter J, Heinle M, Brenner-Weiss-G, Gerthsen D, Nienhaus GU (2014) Nanoparticles interacting with proteins and cells: a systematic study of protein surface charge effects. *Adv Mater Interfaces* 1:1300079
117. Su M, Ye J, Li Q, Ge W, Zhang Y, Jiang H, Amatore C, Wang X (2015) In vivo accurate target bio-marking of tumors through in situ biosynthesized fluorescent zinc nanoclusters. *RSC Adv* 5:74844–74849
118. Chen T, Xu S, Zhao T, Zhu L, Wei D, Li Y, Zhang H, Zhao C (2012) Gold nanocluster-conjugated

- amphiphilic block copolymer for tumor-targeted drug delivery. *ACS Appl Mater Interfaces* 4:5766–5774
119. Chen D, Luo Z, Li N, Lee JY, Xie J, Lu J (2013) Amphiphilic polymeric nanocarriers with luminescent gold nanoclusters for concurrent bioimaging and controlled drug release. *Adv Funct Mater* 23:4324–4331
 120. Chen H, Li B, Ren X, Li S, Ma Y, Cui S, Gu Y (2012) Multifunctional near-infrared-emitting nanoconjugates based on gold clusters for tumor imaging and therapy. *Biomaterials* 33:8461–8476
 121. Cui HD, Hu DH, Zhang JN, Gao GH, Zheng CF, Gong P, Xi XH, Sheng ZH, Cai LT (2017) Theranostic gold cluster nanoassembly for simultaneous enhanced cancer imaging and photodynamic therapy. *Chin Chem Lett* 28:1391–1398
 122. Duan Y, Duan R, Liu R, Guan M, Chen W, Ma J, Chen M, Du B, Zhang Q (2018) Chitosan-stabilized self-assembled fluorescent gold nanoclusters for cell imaging and biodistribution in vivo. *ACS Biomater Sci Eng* 4:1055–1063
 123. Wei Q, Chen Y, Ma X, Ji J, Qiao Y, Zhou B, Ma F, Ling D, Zhang H, Tian M, Tian J, Zhou M (2018) High-efficient clearable nanoparticles for multimodal imaging and image-guided cancer therapy. *Adv Funct Mater* 28:1704634
 124. Zhuang Q, Jia H, Du L, Li Y, Chen Z, Huang S, Liu Y (2014) Targeted surface-functionalized gold nanoclusters for mitochondrial imaging. *Biosens Bioelectron* 55:76–82
 125. Vankayala R, Kuo CL, Nuthalapati K, Chiang CS, Hwang KC (2015) Nucleus-targeting gold nanoclusters for simultaneous in vivo fluorescence imaging, gene delivery, and NIR-light activated photodynamic therapy. *Adv Funct Mater* 25:5934–5945
 126. Chen T, Hu Y, Cen Y, Chu X, Lu Y (2013) A dual-emission fluorescent nanocomplex of gold-cluster-decorated silica particles for live cell imaging of highly reactive oxygen species. *J Am Chem Soc* 135:11595–11602
 127. Chen YN, Chen PC, Wang CW, Lin YS, Ou CM, Ho LC, Chang HT (2014) One-pot synthesis of fluorescent BSA-Ce/Au nanoclusters as ratiometric pH probes. *Chem Commun* 50:8571–8574
 128. Pan S, Zhou J, Liu W, Ye Y, Chen G, Xu J, Qian Z, Chen J, Feng H (2019) Viscosity-sensitive thiolated gold nanoclusters with diffusion-controlled emission for intracellular viscosity imaging. *Analyst* 144:4483–4487
 129. Ma Y, Zhao Y, Guo R, Zhu L, Lin W (2018) A near-infrared emission fluorescent probe with multirotatable moieties for highly sensitive detection of mitochondrial viscosity in an inflammatory cell model. *J Mater Chem B* 6:6212–6216
 130. Yang Z, He Y, Lee JH, Park N, Suh M, Chae WS, Cao J, Peng X, Jung H, Kang C, Kim JS (2013) A self-calibrating bipartite viscosity sensor for mitochondria. *J Am Chem Soc* 135:9181–9185
 131. Gao F, Cai P, Yang W, Xue J, Gao L, Liu R, Wang Y, Zhao Y, He X, Zhao L (2015) Ultrasmall [⁶⁴Cu]Cu nanoclusters for targeting orthotopic lung tumors using accurate positron emission tomography imaging. *ACS Nano* 9:4976–4986
 132. McDonald DM, Baluk P (2002) Significance of blood vessel leakiness in cancer. *Cancer Res* 62:5381–5385
 133. Zhao Y, Detering L, Sultan D, Cooper ML, You M, Cho S, Meier SL, Luehmann H, Sun G, Rettig M, Dehdashti F, Wooley KL, DiPersio JF, Liu Y (2016) Gold nanoclusters doped with ⁶⁴Cu for CXCR4 positron emission tomography imaging of breast cancer and metastasis. *ACS Nano* 10:5959–5970
 134. Hu H, Huang P, Weiss OJ, Yan X, Yue X, Zhang MG, Tang Y, Nie L, Ma Y, Niu G, Wu K, Chen X (2014) PET and NIR optical imaging using self-illuminating ⁶⁴Cu-doped chelator-free gold nanoclusters. *Biomaterials* 35:9868–9876
 135. Zhao Y, Sultan D, Detering L, Luehmann H, Liu Y (2014) Facile synthesis, pharmacokinetic and systemic clearance evaluation, and positron emission tomography cancer imaging of ⁶⁴Cu-Au alloy nanoclusters. *Nanoscale* 6:13501–13509
 136. Shang L, Stockmar F, Azadfar N, Nienhaus GU (2013) Intracellular thermometry by using fluorescent gold nanoclusters. *Angew Chem Int Ed* 52:11154–11157
 137. Wang Y, Chen J, Irudayaraj J (2011) Nuclear targeting dynamics of gold nanoclusters for enhanced therapy of HER2⁺ breast cancer. *ACS Nano* 5:9718–9725
 138. Khandelia R, Bhandari S, Pan UN, Ghosh SS, Chattopadhyay A (2015) Gold nanocluster embedded albumin nanoparticles for two-photon imaging of cancer cells accompanying drug delivery. *Small* 11:4075–4081
 139. Gu W, Zhang Q, Zhang T, Li Y, Xiang J, Peng R, Liu J (2016) Hybrid polymeric nano-capsules loaded with gold nanoclusters and indocyanine green for dual-modal imaging and photothermal therapy. *J Mater Chem B* 4:910–919
 140. Hu D, Sheng Z, Fang S, Wang Y, Gao D, Zhang P, Gong P, Ma Y, Cai L (2014) Folate receptor-targeting gold nanoclusters as fluorescence enzyme mimetic nanoprobes for tumor molecular colocalization diagnosis. *Theranostics* 4:142–153
 141. Qiao J, Mu X, Qi L, Deng J, Mao L (2013) Folic acid-functionalized fluorescent gold nanoclusters with polymers as linkers for cancer cell imaging. *Chem Commun* 49:8030–8032
 142. Pyo K, Ly NH, Yoon SY, Shen Y, Choi SY, Lee SY, Joo SW, Lee D (2017) Highly luminescent folate-functionalized Au₂₂ nanoclusters for bioimaging. *Adv Healthc Mater* 6:1700203
 143. Jiang H, Xu G, Sun Y, Zheng W, Zhu X, Wang B, Zhang X, Wang G (2015) A “turn-on” silver nanocluster based fluorescent sensor for folate

- receptor detection and cancer cell imaging under visual analysis. *Chem Commun* 51:11810–11813
144. Li J, You J, Zhuang Y, Han C, Hu J, Wang A, Xu K, Zhu JJ (2014) A “light-up” and “spectrum-shift” response of aptamer-functionalized silver nanoclusters for intracellular mRNA imaging. *Chem Commun* 50:7107–7110
 145. Chen F, Goel S, Hernandez R, Graves SA, Shi S, Nickles RJ, Cai W (2016) Dynamic positron emission tomography imaging of renal clearable gold nanoparticles. *Small* 12:2775–2782
 146. Zhou C, Hao G, Thomas P, Liu J, Yu M, Sun S, Oz OK, Sun X, Zheng J (2012) Near-infrared emitting radioactive gold nanoparticles with molecular pharmacokinetics. *Angew Chem Int Ed* 51:10118–10122
 147. Chen X, Zhu H, Huang X, Wang P, Zhang F, Li W, Chen G, Chen B (2017) Novel iodinated gold nanoclusters for precise diagnosis of thyroid cancer. *Nanoscale* 9:2219–2231
 148. Liu CL, Wu HT, Hsiao YH, Lai CW, Shih CW, Peng YK, Tang KC, Chang HW, Chien YC, Hsiao JK, Cheng JT, Chou PT (2011) Insulin-directed synthesis of fluorescent gold nanoclusters: preservation of insulin bioactivity and versatility in cell imaging. *Angew Chem Int Ed* 50:7056–7060
 149. Liu Y, Tian GF, He XW, Li WY, Zhang YK (2016) Microwave-assisted one-step rapid synthesis of near-infrared gold nanoclusters for NIRF/CT dual-modal bioimaging. *J Mater Chem B* 4:1276–1283
 150. Sun SK, Dong LX, Cao Y, Sun HR, Yan XP (2013) Fabrication of multifunctional Gd_2O_3/Au hybrid nanoprobe via a one-step approach for near-infrared fluorescence and magnetic resonance multimodal imaging in vivo. *Anal Chem* 85:8436–8441
 151. Liang G, Ye D, Zhang X, Dong F, Chen H, Zhang S, Li J, Shen X, Kong J (2013) One-pot synthesis of Gd^{3+} -functionalized gold nanoclusters for dual model (fluorescence/magnetic resonance) imaging. *J Mater Chem B* 1:3545–3552
 152. Wang C, Yao Y, Song Q (2015) Gold nanoclusters decorated with magnetic iron oxide nanoparticles for potential multimodal optical/magnetic resonance imaging. *J Mater Chem C* 3:5910–5917
 153. Shibu ES, Sugino S, Ono K, Saito H, Nishioka A, Yamamura S, Sawada M, Nosaka Y, Biju V (2013) Singlet-oxygen-sensitizing near-infrared-fluorescent multimodal nanoparticles. *Angew Chem Int Ed* 52:10559–10563
 154. He F, Yang G, Yang P, Yu Y, Lv R, Li C, Dai Y, Gai S, Lin J (2015) A new single 808 nm NIR light-induced imaging-guided multifunctional cancer therapy platform. *Adv Funct Mater* 25:3966–3976
 155. Yang D, Yang G, Gai S, He F, An G, Dai Y, Lv R, Yang P (2015) Au_{25} cluster functionalized metal-organic nanostructures for magnetically targeted photodynamic/photothermal therapy triggered by single wavelength 808 nm near-infrared light. *Nanoscale* 7:19568–19578
 156. Pan UN, Khandelia R, Sanpui P, Das S, Paul A, Chattopadhyay A (2016) Protein-based multifunctional nanocarriers for imaging, photothermal therapy, and anticancer drug delivery. *ACS Appl Mater Interfaces* 9:19495–19501
 157. Hou W, Xia F, Alfranca G, Yan H, Zhi X, Liu Y, Peng C, Zhang C, de la Fuente JM, Cui D (2017) Nanoparticles for multi-modality cancer diagnosis: simple protocol for self-assembly of gold nanoclusters mediated by gadolinium ions. *Biomaterials* 120:103–114
 158. Hu DH, Sheng ZH, Zhang PF, Yang DZ, Liu SH, Gong P, Gao DY, Fang ST, Ma YF, Cai LT (2013) Hybrid gold-gadolinium nanoclusters for tumor-targeted NIRF/CT/MRI triple-modal imaging in vivo. *Nanoscale* 5:1624–1628
 159. Han L, Xia JM, Hai X, Shu Y, Chen XW, Wang JH (2017) Protein-stabilized gadolinium oxide-gold nanoclusters hybrid for multimodal imaging and drug delivery. *ACS Appl Mater Interfaces* 9:6941–6949
 160. Zhao C, Du T, Rehman F, Lai L, Liu X, Jiang X, Li X, Chen Y, Zhang H, Sun Y, Luo S, Jiang H, Selke M, Wang X (2016) Biosynthesized gold nanoclusters and iron complexes as scaffolds for multimodal cancer bioimaging. *Small* 12:6255–6265
 161. Xu C, Wang Y, Zhang C, Jia Y, Luo Y, Gao X (2017) AuGd integrated nanoprobe for optical/MRI/CT triple-modal in vivo tumor imaging. *Nanoscale* 9:4620–4628
 162. Wu X, Li C, Liao S, Li L, Wang T, Su Z, Wang C, Zhao J, Sui C, Lin J (2014) Silica-encapsulated Gd^{3+} -aggregated gold nanoclusters for in vitro and in vivo multimodal cancer imaging. *Chem Eur J* 20:8876–8882
 163. Hembury M, Chiappini C, Bertazzo S, Kalber TL, Drisko GL, Ogunlade O, Walker-Samuel S, Krishna KS, Jumeaux C, Beard P, Kumar CS, Porter AE, Lythgoe MF, Boissiere C, Sanchez C, Stevens MM (2015) Gold-silica quantum rattles for multimodal imaging and therapy. *Proc Natl Acad Sci U S A* 112:1959–1964
 164. Shen D, Henry M, Trouillet V, Comby-Zerbino C, Bertorelle F, Sancey L, Antoine R, Coll JL, Josserand V, Le Guével X (2017) Zwitterion functionalized gold nanoclusters for multimodal near infrared fluorescence and photoacoustic imaging. *APL Mater* 5:053404
 165. Jin R, Zeng C, Zhou M, Chen Y (2016) Atomically precise colloidal metal nanoclusters and nanoparticles: fundamentals and opportunities. *Chem Rev* 116:10346–10413
 166. Wang S, Meng X, Das A, Li T, Song Y, Cao T, Zhu X, Zhu M, Jin R (2014) A 200-fold quantum yield boost in the photoluminescence of silver-doped Ag_xAu_{25-x} nanoclusters: the 13 th silver atom matters. *Angew Chem Int Ed* 53:2376–2380
 167. Shang L, Nienhaus GU (2017) Research Update: Interfacing ultrasmall metal nanoclusters with biological systems. *APL Mater* 5:053101